RADIATIVE TRANSFER IN THE ATMOSPHERE-SNOW-ICE-WATER SYSTEM:

TECHNICAL DESCRIPTION OF THE AccuRT COMPUTATIONAL CODE

Contents

1 Introduction

Reliable, accurate, and efficient modeling of electromagnetic radiation transport in turbid media has important applications in studies of Earth's climate by remote sensing. For example, such modeling is needed to develop forward-inverse methods used to quantify types and concentrations of aerosol and cloud particles in the atmosphere, as well as dissolved organic and particulate biogeochemical matter in lakes, rivers, coastal, and open-ocean waters, and to simulate the performance of remote sensing detectors deployed on aircraft, balloons, and satellites. Accurate radiative transfer modeling is also required to compute irradiances and scalar irradiances that are used to compute warming/cooling and photolysis rates in the atmosphere, solar energy disposition in the cryosphere including frozen fresh water (lakes and rivers), sea ice, and glaciers, as well as primary production rates in the water.

Accurate, efficient, and easy-to-use radiative transfer (RT) simulation tools, such as **AccuRT**, are important because they (i) can be used to generate irradiances at any user-specified location in the atmosphere-water system as well as radiances at any user-specified location and direction for user-specified inherent optical properties (**IOP**s); (ii) will provide accurate results for given input parameters; (iii) will prevent time being wasted on developing tools that in comparison with **AccuRT** may be less reliable, less general, and more prone to produce erroneous results that may be difficult to spot; (iv) will lead to significant progress in research areas such as remote sensing algorithm development, climate research, and other atmospheric and hydrologic applications.

Currently available tools for atmospheric applications include: (i) SBDART, Streamer, and LibRadtran, which apply to the atmosphere only; there is no coupling to the underlying surface including solid (snow/ice) and liquid water – surface input is a boundary condition; (ii) Hydrolight, which applies to ocean (natural waters) only, provides water-leaving radiance, but no top-of-the-atmosphere (TOA)

radiance; there is no coupling to the atmosphere – atmospheric input is a boundary condition. Therefore, **AccuRT** was designed to provide a reliable, well-tested, robust, versatile, and easy-to-use RT tool for coupled systems. This document describes the **AccuRT** tool for RT simulations in atmosphere-water systems consisting of two slabs with different refractive indices. Note that in this document the word "water" is frequently used generically to describe the solid phase (*i.e.* snow and ice) as well as the liquid phase. The computer code **AccuRT** accounts for reflection and transmission at the interface between the two slabs, and allows for each slab to be divided into a number of layers sufficiently large to resolve the variation in the inherent optical properties (**IOP**s) with depth in each slab.

1.1 Notation

Radiative transfer practitioners in the atmosphere, water (ocean) and cryosphere (snow/ice) communities use different nomenclatures and terminologies. This situation can be confusing and frustrating to students and researchers alike who are addressing interdisciplinary problems in environmental optics where radiative transfer in both the atmosphere and the underlying surface are important. To alleviate this state of affairs we will adopt the notation of Stamnes and Stamnes (2015) [1] throughout this document (z is the vertical position in the plane-parallel medium under consideration, Θ is the scattering angle, and ϕ is the azimuth angle):

1. the absorption coefficient will be denoted by the Greek letter $\alpha(z)$ in units of $[\mathrm{m}^{-1}]$;
2. the scattering coefficient will be denoted by the Greek letter $\beta(z)$ in units of $[\mathrm{m}^{-1}]$;
3. the extinction coefficient will be denoted by the Greek letter $\gamma(z) = \alpha(z)+\beta(z)$ in units of $[\mathrm{m}^{-1}]$;
4. the corresponding cross sections in units of $[\mathrm{m}^2]$ will be denoted by a subscript n: $\alpha_{\mathrm{n}}(z), \beta_{\mathrm{n}}(z), \gamma_{\mathrm{n}}(z)$;
5. the volume scattering function will be denoted by $\mathrm{vsf}(z, \cos\Theta, \phi)$ in units of $[\mathrm{m}^{-1}\mathrm{sr}^{-1}]$;
6. the single-scattering albedo will be denoted by $\varpi(z) = \beta(z)/(\alpha(z) + \beta(z))$.

The corresponding notation used in the Ocean Optics community is a instead of α, b instead of β, and c instead of γ. Since α, β, and γ are the 3 first letters in the greek alphabet it should be easy to recall the connection with a, b, and c.

2 User Interface – Input/Output

The **AccuRT** tool is user-friendly so that the user only needs to specify the physical input required and the output desired.

2.1 Input parameters

The user must specify the physical properties of each of the two slabs that constitute the coupled system, the radiative energy input at the top of the upper slab (top-of-the-atmosphere, TOA), and the boundary conditions at the bottom of the lower slab (water bottom). Each of the two slabs is assumed to be a plane-parallel, vertically stratified structure in which the scattering and absorption properties, *i.e.* the inherent optical properties (**IOP**s) defined in Section 3 below, are allowed to vary only in the vertical direction, denoted by z. In order to resolve changes in the **IOP**s as a function of vertical position z, each slab is divided into a number of adjacent horizontal layers such that the **IOP**s are constant within each layer, but allowed to vary from one layer to the next. The atmosphere-water interface is assumed to be flat in the present version of **AccuRT**. A wind-roughened interface will be included in an upcoming version.

To facilitate the specification of **IOP**s in the atmosphere-water system, **AccuRT** uses the concept of **materials**, which are radiatively-significant constituents in the atmosphere-water system. Examples of currently available materials are **aerosols**, **earth_atmospheric_gases**, **clouds**, **snow**, **ice**, **water_impurity_ccrr** and **pure_water**. These materials automatically account for the wavelength dependence of the **IOP**s so that all the user needs to do is to decide upfront – in the **main** configuration file – which of these materials to include in each horizontal layer.

The user must specify:

1. beam irradiance in [W m^{-2}] – a default solar spectrum is available (**main** configuration file);
2. wavelength range, # of center wavelengths and widths in [nm] – a discrete set of wavelengths is allowed (**main** configuration file);
3. solar zenith angle(s) in degrees (**main** configuration file);
4. the number of "discrete ordinate streams" used to solve the radiative transfer equation (RTE) as described in Section 4 (**main** configuration file);
5. materials used (**main** configuration file).

Specifications required for the upper slab:

1. layer boundaries, ground-level altitude (sea-level is default) defined in Section 3.3.3 (**main** configuration file);
2. atmospheric type (atmNo, defined in Section 3.3.3) (**earth_atmospheric_gases** configuration file);
3. aerosol particle types (a bi-modal log-normal volume distribution is allowed) for each layer defined in Section 3.3.4 (**aerosols** configuration file);
4. cloud particles as described in Section 3.3.5 (**clouds** configuration file);

5. snow particles as described in Section 3.4 (**snow** configuration file);

Specifications required for the lower slab:

1. layer boundaries (**main** configuration file);
2. ice material as described in Section 3.4 (**ice** configuration file);
3. refractive index as a function of wavelength in the lower slab (water) – set to "one" in the upper slab (atmosphere) (**pure_water** configuration file);
4. water impurities (**water_impurity_ccrr** configuration file);
5. water bottom albedo and emissivity (**main** configuration file).

2.2 Spectral input and resolution

The input solar spectrum at the TOA is ATLAS3 (shifted to air wavelengths) for $200 < \lambda < 407$ nm, ATLAS2 for $407.8 < \lambda < 419.9$ nm, and MODTRAN (v3.5) for $419.9 < \lambda < 800$ nm. Between 200 and 800 nm the solar irradiance has a spectral resolution of 0.05 nm. For $\lambda > 800$ nm (http://rredc.nrel.gov/solar/spectra/am1.5/ASTMG173/ASTMG173.html) the ASTM G173-03 spectrum is adopted with a spectral resolution of 1 nm between 800 and 1,700 nm and 5 nm between 1,700 and 4,000 nm.

2.3 Output parameters

Once the input parameters specified above have been defined, the **AccuRT** code will solve the RTE as described in Section 4, and provide two types of output:

- irradiances and mean intensities (scalar irradiances) at a set of user-specified vertical positions in the coupled system;
- radiances in a number of user-specified directions at a set of user-specified vertical positions in the coupled system.

Thus, the user specifies:

1. the vertical positions at which output is desired (**main** configuration file);
2. the type of output (**main** configuration file):
   - hemispherical and scalar irradiances only;
   - radiances only;
   - hemispherical and scalar irradiances as well as radiances;
3. the directions in which radiances are requested (**main** configuration file).

3 Inherent Optical Properties (IOPs)

3.1 General Definitions

The optical properties of a medium can be categorized as inherent or apparent. An *inherent optical property* (IOP) depends only on the medium itself, and *not* on the ambient light field within the medium [2]. An *apparent optical property* (AOP) depends also on the illumination, *i.e.* on light propagating in particular directions inside and outside the medium*.

The absorption coefficient $\alpha(z)$ and the scattering coefficient $\beta(z)$ are important IOPs, defined as [3]

$$\alpha(z) = \frac{1}{I^i}\left(\frac{dI^\alpha}{dz}\right) \qquad [\mathrm{m}^{-1}] \tag{1}$$

$$\beta(z) = \frac{1}{I^i}\left(\frac{dI^\beta}{dz}\right) \qquad [\mathrm{m}^{-1}]. \tag{2}$$

Here I^i is the incident radiance entering a volume element $dV = dA\,dz$ of the medium of cross sectional area dA and thickness dz, and $dI^\alpha > 0$ and $dI^\beta > 0$ are respectively the radiances that are absorbed and scattered in all directions as the light propagates the distance dz, which is the thickness of the volume element dV along the direction of the incident light. If the distance dz is measured in [m], the unit for the absorption or scattering coefficients defined in Eq. (1) and Eq. (2) becomes $[\mathrm{m}^{-1}]$.

The angular distribution of the scattered light is given in terms of the *volume scattering function* (vsf), which is defined as

$$\mathrm{vsf}(z, \hat{\mathbf{\Omega}}', \hat{\mathbf{\Omega}}) = \frac{1}{I^i}\frac{d^2 I^\beta}{dz\,d\omega} = \frac{1}{I^i}\frac{d}{dz}\left(\frac{dI^\beta}{d\omega}\right) \qquad [\mathrm{m}^{-1}\,\mathrm{sr}^{-1}]. \tag{3}$$

Here $\hat{\mathbf{\Omega}}'$ and $\hat{\mathbf{\Omega}}$ are unit vectors, and $d^2 I^\beta$ is the radiance scattered from an incident direction $\hat{\mathbf{\Omega}}'$ into a cone of solid angle $d\omega$ around the direction $\hat{\mathbf{\Omega}}$ as the light propagates the distance dz along the direction $\hat{\mathbf{\Omega}}'$. The plane spanned by $\hat{\mathbf{\Omega}}'$ and $\hat{\mathbf{\Omega}}$ is called the *scattering plane*, and the *scattering angle* Θ is given by $\cos\Theta = \hat{\mathbf{\Omega}}' \cdot \hat{\mathbf{\Omega}}$. Integration of Eq. (3) over all scattering directions yields

$$\begin{aligned}\beta(z) &= \frac{1}{I^i}\frac{d}{dz}\int_{4\pi}\left(\frac{dI^\beta}{d\omega}\right)d\omega = \frac{1}{I^i}\left(\frac{dI^\beta}{dz}\right) \\ &= \int_{4\pi}\mathrm{vsf}(z, \hat{\mathbf{\Omega}}', \hat{\mathbf{\Omega}})\,d\omega = \int_0^{2\pi}\int_0^{\pi}\mathrm{vsf}(z, \cos\Theta, \phi)\sin\Theta\,d\Theta\,d\phi \qquad [\mathrm{m}^{-1}]\end{aligned} \tag{4}$$

*Apparent optical properties (1) depend both on the medium (the IOPs) and on the geometric (directional) structure of the radiance distribution, and (2) display enough regular features and stability to be useful descriptors of a water body [2]. Hence, a radiance or an irradiance would satisfy only the first part of the definition, while a radiance or irradiance reflectance, obtained by division of the radiance or the upward irradiance by the downward irradiance, would satisfy also the second part of the definition.

where Θ and ϕ are respectively the polar angle and the azimuth angle in a spherical coordinate system in which the polar axis is along $\hat{\mathbf{\Omega}}'$. As indicated in Eq. (4), the vsf $[\mathrm{vsf}(z, \cos\Theta, \phi)]$ is generally a function of both Θ and ϕ, but for randomly oriented scatterers one may assume that the scattering potential is spherically symmetric implying that there is no azimuthal dependence, so that $\mathrm{vsf} = \mathrm{vsf}(z, \cos\Theta)$. Then one finds, with $x = \cos\Theta$

$$\beta(z) = 2\pi \int_0^\pi \mathrm{vsf}(z, \cos\Theta) \sin\Theta \, d\Theta = 2\pi \int_{-1}^1 \mathrm{vsf}(z, x) \, dx \qquad [\mathrm{m}^{-1}]. \tag{5}$$

A normalized vsf, denoted by $p(z, \cos\Theta)$ and referred to hereafter as the *scattering phase function*, may be defined as follows

$$p(z, \cos\Theta) = 4\pi \frac{\mathrm{vsf}(z, \cos\Theta)}{\int_{4\pi} \mathrm{vsf}(z, \cos\Theta) \, d\omega} = \frac{\mathrm{vsf}(z, \cos\Theta)}{\frac{1}{2}\int_{-1}^1 \mathrm{vsf}(z, \cos\Theta) \, d(\cos\Theta)}, \tag{6}$$

so that

$$\frac{1}{4\pi} \int_{4\pi} p(z, \cos\Theta) \, d\omega = \frac{1}{2} \int_{-1}^1 p(z, x) \, dx = 1. \tag{7}$$

The scattering phase function has the following physical interpretation. Given that a scattering event has occurred, $p(z, \cos\Theta) \, d\omega/4\pi$ is the probability that a light beam traveling in the direction $\hat{\mathbf{\Omega}}'$ is scattered into a cone of solid angle $d\omega$ around the direction $\hat{\mathbf{\Omega}}$.

The scattering phase function $[p(z, \cos\Theta)]$ describes the angular distribution of the scattered light, while the scattering coefficient $\beta(z)$ describes the total amount of scattered light integrated over all scattering directions. A convenient measure of the "shape" of the scattering phase function is the average over all scattering directions (weighted by $p(z, \cos\Theta)$) of the cosine of the scattering angle Θ, *i.e.*

$$\begin{aligned} g(z) = \langle \cos\Theta \rangle &= \frac{1}{4\pi} \int_{4\pi} p(z, \cos\Theta) \, \cos\Theta \, d\omega \\ &= \frac{1}{2} \int_0^\pi p(z, \cos\Theta) \, \cos\Theta \, \sin\Theta \, d\Theta = \frac{1}{2} \int_{-1}^1 p(z, \cos\Theta) \cos\Theta \, d(\cos\Theta). \end{aligned} \tag{8}$$

The average cosine $g(z)$ is called the *asymmetry factor* of the scattering phase function. Equation (8) yields complete forward scattering if $g = 1$, complete backward scattering if $g = -1$, and $g = 0$ if $p(z, \cos\Theta)$ is symmetric about $\Theta = 90°$. Thus, isotropic scattering also gives $g = 0$. Similarly, the probability of scattering into the backward hemisphere, is given by the backscattering ratio (or backscatter fraction) b, defined as

$$b(z) = \frac{1}{2} \int_{\pi/2}^\pi p(z, \cos\Theta) \, \sin\Theta \, d\Theta = \frac{1}{2} \int_0^1 p(z, -x) \, dx. \tag{9}$$

The scattering phase function $p(z, \cos\Theta)$ depends on the refractive index as well as the size and shape of the scattering particles, and will thus depend on the physical situation and the practical application of interest. Two different scattering phase functions, which are useful in practical applications, are discussed below.

3.2 Types of Scattering Phase Functions

3.2.1 Rayleigh Scattering Phase Function

When the size d of the scatterers is small compared with the wavelength of light ($d < \frac{1}{10}\lambda$), the Rayleigh scattering phase function gives a good description of the angular distribution of the scattered light. The Rayleigh scattering phase function for unpolarized light is given by

$$p(\cos\Theta) = \frac{3}{3+f}(1 + f\cos^2\Theta) \tag{10}$$

where the parameter $f = \frac{1-\rho}{1+\rho}$, and ρ is the depolarization ratio, attributed to the anisotropy of the scatterer (molecule) [4, 5, 6, 7]. Originally this scattering phase function was derived for light radiated by an electric dipole [8]. Since the Rayleigh scattering phase function is symmetric about $\Theta = 90°$, the asymmetry factor is $g = 0$. If the Rayleigh scattering phase function is expanded in Legendre polynomials, the expansion coefficients χ_ℓ [see Eq. (85) below] are simply given by $\chi_0 = 1$, $\chi_1 = 0$, $\chi_2 = \frac{2f}{5(3+f)}$, and $\chi_\ell = 0$ for $\ell > 2$.

Using $\rho = 0.04$ for air, we get $f = \frac{1-\rho}{1+\rho} = 0.923$, and using $\rho = 0.09$ for water, we get $f = \frac{1-\rho}{1+\rho} = 0.835$. Hence, for Rayleigh scattering the phase function moments become:

- $\chi_0 = 1$, $\chi_1 = 0$, $\chi_2 = 0.0941$ and $\chi_\ell = 0$ for $\ell > 2$ for air, and
- $\chi_0 = 1$, $\chi_1 = 0$, $\chi_2 = 0.0871$, and $\chi_\ell = 0$ for $\ell > 2$ for water.

3.2.2 Henyey-Greenstein Scattering Phase Function

In 1941 Henyey and Greenstein [9] proposed the one-parameter scattering phase function given by [oppressing the dependence on the position z]

$$p(\cos\Theta) = \frac{1-g^2}{(1+g^2-2g\,\cos\,\Theta)^{3/2}} \tag{11}$$

where the parameter g is the asymmetry factor defined in Eq. (8). The Henyey–Greenstein (HG) scattering phase function has no physical basis, but is very useful for describing a highly scattering medium, such as turbid water or sea ice, for which the actual scattering phase function is unknown. The HG scattering phase function is convenient for Monte Carlo simulations and other numerical calculations because it has an analytical form. In deterministic plane-parallel RT models it is also very convenient because the addition theorem of spherical harmonics can be used to expand the scattering phase function in a series of Legendre polynomials [1, 3], as reviewed in Section 4.1.1. For the HG scattering phase function, the expansion coefficients χ_ℓ in this series [see Eq. (85) below] are simply given by $\chi_\ell = g^\ell$, where $g = \chi_1$ is the asymmetry factor defined in Eq. (8). The HG scattering phase function is useful for scatterers with sizes comparable to or larger than the wavelength of light.

3.3 Atmosphere

The stratified vertical structure of the bulk properties of an atmosphere is a consequence of hydrostatic balance. For an atmosphere in a state of rest, the pressure $p(z)$ must support the weight of the fluid above it. By equating pressure forces and gravitational forces, one finds that $dp(z) = -g\ \rho(z)\ dz$ where g is the acceleration due to gravity (assumed to be constant), $\rho(z)$ is the air density, and dp is the differential change in pressure over the small height interval dz. Combining $dp(z) = -g\rho(z)$ with (i) the ideal gas law $p(z) = n(z)kT(z)$, where k is Boltzmann's constant and $n(z) = N/V(z)$ with V being the volume of a gas at temperature T containing N molecules, and (ii) $\rho(z) = \bar{M}n(z)$, where $\bar{M}$ is the mean molecular weight, one finds $\frac{dp(z)}{p(z)} = -\frac{dz}{H(z)}$, where $H(z) = kT(z)/\bar{M}g$ is the atmospheric scale height. Upon integration, one finds

$$p(z) = p(z_0) \exp\Big[-\int_{z_0}^{z} dz'/H(z')\Big]. \tag{12}$$

The ideal gas law allows us to write similar expressions for the density $\rho(z)$ and the concentration $n(z)$. Clearly, from a knowledge of the surface pressure $p(z_0)$ and the variation of the scale height $H(z)$ with height z, Eq. (12) allows us to determine the bulk gas properties at any height. Equation (12) applies to well-mixed gases, but not to short-lived species such as ozone, which is chemically created and destroyed, or water, which undergoes phase changes on short time scales. Assuming that g, T, and $\bar{M}$ (and hence H) are constants, we may integrate Eq. (12) to obtain:

$$\frac{p(z)}{p(z_0)} \approx e^{-(z-z_0)/H}, \qquad \frac{n(z)}{n(z_0)} \approx e^{-(z-z_0)/H}, \qquad \frac{\rho(z)}{\rho(z_0)} \approx e^{-(z-z_0)/H}. \tag{13}$$

Thus, the scale height H is an e-fold height for density.

Going back to the ideal gas law: $pV = NkT \Leftrightarrow pDA = NkT$, where A is the area of a vertical column, and D its height, we may define an **equivalent depth** as:

$$D \equiv \frac{\mathcal{N}kT}{p}. \tag{14}$$

where $\mathcal{N} = N/A$ is the column amount [molecules m^{-2}].

3.3.1 Gases in the Earth's atmosphere

The total number of air molecules in a 1 m^2 wide vertical column extending from sea level to the top of the atmosphere is about 2.15×10^{29}. In comparison, the total column amount of ozone in the same vertical column is about 1.0×10^{23}. The equivalent depth in millicentimeters (10^{-5} m) that a layer of ozone gas in the atmosphere would occupy if it were compressed to standard pressure (1,013 [hP]; 1 hP (hectoPascal) = 1 N m^{-2}) at standard temperature (0 °C) is called the Dobson unit (DU). Thus, one DU refers to a layer of ozone that would be 10 μm = 10^{-5} m thick under standard temperature and pressure. The conversion is 1 DU = 2.69×10^{20} molecules m^{-2}. The 1976 US Standard Atmosphere contains about 348 DU of ozone gas [10].

AccuRT has a material called **earth_atmospheric_gases** that allows the user to choose between the six model atmospheres described by Anderson et al. (1986) [10]. These model atmospheres are included in a band model based on LowTran/ModTran, and they are tabulated in Appendix C in Thomas and Stamnes (1999) [3] as follows:
Table C1: AFGL atmospheric constituent profiles, US Standard atmosphere 1976
Table C2: AFGL atmopsheric constituent profiles, tropical
Table C3: AFGL atmospheric constituent profiles, midlatitude summer
Table C4: AFGL atmospheric constituent profiles, midlatitude winter
Table C5: AFGL atmospheric constituent profiles, subarctic summer
Table C6: AFGL atmospheric constituent profiles, subarctic winter.

These atmospheric models are based on the best data available when they were published [10], and they contain profiles of temperature, pressure and concentrations of several gaseous constituents including H_2O, CO_2, O_3, CH_4, and NO_2. These five species are the most important infrared-significant gases in the Earth's atmosphere.

The clear atmosphere (no clouds or aerosols) molecular scattering and gaseous absorption coefficients as a function of wavelength and level in the atmosphere are generated as specified below. Corresponding scattering and absorption coefficients for aerosol particles are also given below.

3.3.2 Vertical Structure

The atmosphere is divided into a sufficient number of layers to resolve the vertical variation in the IOPs. A default vertical structure is provided in the `main` configuration file.

3.3.3 Molecular IOPs

The earth_atmospheric_gases material
The **earth_atmospheric_gases material** provides specification of absorption coefficients $\alpha(\lambda)$ (or cross sections $\alpha_n(\lambda)$) for the radiatively-significant atmospheric gases including ozone and water vapor. Currently there are two options: the user may select either the **gasIOP** material or the **Air** material, both of which are defined below. A specification with moderate spectral resolution based on "fixed-wavenumber" sampling of 1 cm^{-1} (and a nominal resolution of 2 cm^{-1}), is sufficient for many purposes, because the radiative transfer process is assumed to be "quasi-monochromatic" within this spectral band [3]. For wavenumbers larger than $17,905\,\mathrm{cm}^{-1}$ ($\lambda < 558.5\,\mathrm{nm}$), we use a lower spectral resolution of $20\,\mathrm{cm}^{-1}$, for which the radiative transfer process is assumed to be "quasi-monochromatic" [3].

The gasIOP material for spectral absorption and scattering
The material called **gasIOP** provides computation of absorption coefficients for gases based on the LowTran/ModTran band model. The **gasIOP** material also provides computation of molecular (Rayleigh) scattering coefficients. The user only

needs to specify the spectral interval of interest and the spectral resolution in [nm] or a set of discrete wavelength bands as discussed above, in the **main** configuration file.

The Air material for spectral absorption and scattering

Alternatively, for wavelengths in the ultraviolet and visible spectral ranges, one may use number density profiles of gas absorption cross sections to compute absorption coefficients, and the total amount of molecules to compute Rayleigh (molecular) scattering coefficients. In the current version of the **Air** material, which includes only ozone absorption in addition to molecular scattering, the atmosphere is essentially transparent for wavelengths longer than 900 nm, where Rayleigh scattering and ozone absorption is negligible. The **Air** option is useful for applications in which only ozone absorption is deemed to important.

3.3.4 Aerosol IOPs (see aerosols material)

If we know the size distribution and the refractive index of the aerosol particles, we may use available aerosol models to generate aerosol **IOPs**. One option is to use the aerosol models employed in the Sea-viewing Wide Field-of-view Sensor (**SeaWiFS**) Database Analysis System (**SeaDAS**), and described by Ahmad et al. (2010) [11]. Another option is to use the OPAC models described by Hess et al. (1998) [12]. For atmospheric correction of ocean color imagery, Gordon and co-workers [13, 14] selected 16 candidate aerosol models consisting of several types of particles, each having its own characteristic chemical composition, size distribution, and hygroscopicity.

It is customary to assume a log-normal distribution of aerosol sizes as proposed by Davies (1974) [15]. Based on AERONET data (Holben et al., 1998, 2001 [16, 17]), Ahmad et al. (2010) [11] adopted a bi-modal log-normal volume size distribution:

$$v(r) = \frac{dV(r)}{dr} = \frac{1}{r}\frac{dV(\ln r)}{d\ln r} = \sum_{i=1}^{2} \frac{V_i}{\sqrt{2\pi}\sigma_i}\frac{1}{r}\exp\left[-\left(\frac{\ln r - \ln r_{\mathrm{v}i}}{\sqrt{2}\sigma_i}\right)^2\right] \tag{15}$$

where the subscript i represents the mode, V_i is the total volume of particles with mode i, $r_{\mathrm{v}i}$ is the mode radius, also called the volume geometric mean radius, and σ_i is the geometric standard deviation. Note that since the numerator in the exponential of Eq. (15), $\ln(r/r_{\mathrm{v}i})$, is dimensionless, so is σ_i. Since

$$\int_0^\infty \frac{dr}{\sqrt{2\pi}\sigma}\frac{1}{r}\exp\left[-\left(\frac{\ln r - \ln r_{\mathrm{v}}}{\sqrt{2}\sigma}\right)^2\right] = 1$$

integration over all sizes for both modes, yields:

$$\int_0^\infty v(r)\,dr = V_1 + V_2 = V.$$

In terms of the number density, Eq. (15) becomes

$$n(r) = \frac{dN(r)}{dr} = \frac{1}{r}\frac{dN(r)}{d(\ln r)} = \sum_{i=1}^{2} \frac{N_i}{\sqrt{2\pi}\sigma_i}\frac{1}{r}\exp\left[-\left(\frac{\ln r - \ln r_{\mathrm{n}i}}{\sqrt{2}\sigma_i}\right)^2\right] \tag{16}$$

where the number of particles N_i and the mean geometric (or mode) radius r_{ni} are related to V_i and r_{vi} as follows

$$\ln r_{ni} = \ln r_{vi} - 3\sigma_i^2 \tag{17}$$

$$N_i = \frac{V_i}{\frac{4}{3}\pi r_{ni}^3} \exp(-4.5\sigma_i^2), \tag{18}$$

and integration over all sizes for both modes, yields:

$$\int_0^\infty n(r)\, dr = N_1 + N_2 = N.$$

If we use the subscript $i = f$ to denote the fine mode, and the subscript $i = c$ to denote the coarse mode, we have $V = V_f + V_c$, and the volume fraction of fine mode particles becomes $f_v = V_f/V$.

A change in the relative humidity (RH) will affect the size of the particle as well as the refractive index. The particle radius can be determined as a function of RH from the wet-to-dry mass ratio:

$$r(a_w) = r_0\left[1 + \rho\frac{m_w(a_w)}{m_0}\right]^{1/3} \tag{19}$$

where the water activity a_w of a soluble aerosol at radius r [μm] can be expressed as

$$a_w = \mathrm{RH} \exp\left[\frac{-2\sigma V_m}{R_w T}\frac{1}{r(a_w)}\right]. \tag{20}$$

Here r_0 is the dry particle radius (RH = 0), ρ is the particle density relative to that of water, $m_w(a_w)$ is the mass of condensed water, m_0 is the dry particle mass (RH = 0), σ is the surface tension on the wet surface, V_m is the specific volume of water, R_w is the gas constant for water vapor, and T is the absolute temperature [K] (Hänel, 1976 [18]). Similarly, the change in refractive index with RH can be determined from (Hänel, 1976 [18])

$$\tilde{m}_c = \tilde{m}_{c,w} + (\tilde{m}_{c,0} - \tilde{m}_{c,w})\left[\frac{r_0}{r_{RH}}\right]^3 \tag{21}$$

where $\tilde{m}_{c,w}$ and $\tilde{m}_{c,0}$ are the complex refractive indices of water and dry aerosols, respectively, and r_0 and r_{RH} are the radii of the aerosols in the dry state and at the given RH, respectively. From these formulas we note that the magnitude of the particle growth and the change of refractive index with increasing RH depend on the size r_0 of the dry aerosol but also on the type of aerosol through the water uptake [the ratio $m_w(a_w)/m_0$ in Eq. (19)] (Hänel, 1976 [18], Shettle and Fenn, 1979 [19], Yan et al., 2002 [20]).

Relationship between effective radius and mode radius

The particle size distribution may also be characterized by an effective radius

$$r_{eff} = \frac{\int_{r_{min}}^{r_{max}} n(r) r^3\, dr}{\int_{r_{min}}^{r_{max}} n(r) r^2\, dr} \tag{22}$$

and an effective variance

$$v_{\text{eff}} = \frac{\int_{r_{\min}}^{r_{\max}} (r - r_{\text{eff}})^2 n(r) r^2 \, dr}{r_{\text{eff}}^2 \int_{r_{\min}}^{r_{\max}} n(r) r^2 \, dr} \tag{23}$$

where r_{eff}^2 is included in the denominator of Eq. (23) to make v_{eff} dimensionless (Hansen and Travis, 1974 [21]). The effective radius, r_{eff}, can be used to describe the IOPs in an approximate manner as will be discussed below for cloud as well as snow/ice materials. For a single mode, the lognormal size distribution is given by [see Eq. (16)]

$$n(r) = \frac{dN(r)}{dr} = \frac{N}{\sqrt{2\pi}\sigma} \frac{1}{r} \exp\left[- \left(\frac{\ln r - \ln r_{\text{n}}}{\sqrt{2}\sigma} \right)^2 \right]$$

where r_{n} is the mode radius, $n(r)$ is the number density or PSD in units of $[\text{m}^{-3} \cdot \text{m}^{-1}]$ and $N = \int_0^\infty n(r) \, dr$ $[\text{m}^{-3}]$ is the total number of particles per unit volume since

$$\int_0^\infty \frac{dr}{\sqrt{2\pi}\sigma} \frac{1}{r} \exp\left[- \left(\frac{\ln r - \ln r_n}{\sqrt{2}\sigma} \right)^2 \right] = 1. \tag{24}$$

With the change of variable $x = \frac{\ln(r/r_{\text{n}})}{\sqrt{2}\sigma}$, Eq. (24) becomes

$$\frac{1}{\sqrt{\pi}} \int_{-\infty}^{+\infty} \exp(-x^2) \, dx = 1. \tag{25}$$

To determine how the effective radius r_{eff} is related to the mode radius r_{n}, we make the change of integration variable $x = \frac{1}{\sqrt{2}\sigma} \ln(r/r_{\text{n}})$ in Eq. (22), so that $dx = \frac{1}{\sqrt{2}\sigma} \frac{dr}{r}$ and $\exp[\sqrt{2}\sigma x] = \frac{r}{r_{\text{n}}}$. Further we have

$$x_{\max} = \frac{1}{\sqrt{2}\sigma} \ln(r_{\max}/r_{\text{n}}) \to +\infty \text{ when } r_{\max} \to +\infty$$
$$x_{\min} = \frac{1}{\sqrt{2}\sigma} \ln(r_{\min}/r_{\text{n}}) \to -\infty \text{ when } r_{\min} \to 0.$$

Thus, Eq. (22) becomes

$$r_{\text{eff}} = r_{\text{n}} \frac{\int_{-\infty}^{+\infty} \exp[-(x^2 - 3\sqrt{2}\sigma x)] dx}{\int_{-\infty}^{+\infty} \exp[-(x^2 - 2\sqrt{2}\sigma x)] dx} \tag{26}$$

which on completing the square in each of the exponents and making use of Eq. (25) leads to

$$r_{\text{eff}} = r_{\text{n}} \exp[2.5\sigma^2]. \tag{27}$$

Proceeding in a similar manner, one finds that the effective variance v_{eff} is related to the variance σ^2 as follows [21]:

$$v_{\text{eff}} = \exp[\sigma^2] - 1. \tag{28}$$

IOPs of a polydispersion – Integrating over the size distribution

Assuming that the aerosols consist of spherical particles and that we have computed the IOPs for a particle with specified refractive index and a given size, we may compute the absorption and scattering coefficients and the scattering phase function for a polydispersion of particles by integrating over the size distribution:

$$\alpha_{\mathrm{p}}(\lambda) = \int_{r_{\min}}^{r_{\max}} \pi r^2 Q'_{\alpha}(r) n(r)\, dr \tag{29}$$

$$\beta_{\mathrm{p}}(\lambda) = \int_{r_{\min}}^{r_{\max}} \pi r^2 Q'_{\beta}(r) n(r)\, dr \tag{30}$$

$$p_{\mathrm{p}}(\lambda, \Theta) = \frac{\int_{r_{\min}}^{r_{\max}} p_{\mathrm{p}}(\lambda, \Theta, r) n(r)\, dr}{\int_{r_{\min}}^{r_{\max}} n(r)\, dr} \tag{31}$$

where

- the absorption or scattering "efficiency", respectively $Q'_{\alpha}(r)$ or $Q'_{\beta}(r)$, is defined as the ratio of the absorption or scattering cross section for a spherical particle of radius r to the geometrical cross section πr^2,
- $n(r)$ is the particle size distribution, and r is the radius of each particle.

aerosols material

The **aerosols** material provides a user-friendly way to specify the aerosol properties as a function of wavelength. The user specifies the location of the aerosols as well as the refractive index of the two modes, the effective radii, and the variances; the rest is taken care of automatically with linear interpolation between wavelengths. A Mie code ([22, 23]) is used to compute the **IOP**s of aerosol particles [$Q'_{\alpha}(r), Q'_{\beta}(r)$, and $p_{\mathrm{p}}(\lambda, \Theta, r)$ in Eqs. (29)–(31)], and a numerical integration is employed to integrate over the log-normal size distributions to obtain $\alpha_{\mathrm{p}}(\lambda), \beta_{\mathrm{p}}(\lambda)$, and $p_{\mathrm{p}}(\lambda, \Theta)$. Finally, the moment-fitting algorithm of Hu et al. (2000) [24] is used to compute Legendre expansion coefficients [see Eq. (85)] $\chi_{\ell,\mathrm{Mie}}$ for the Mie scattering phase function.

In the current version of the **aerosols** material, Eq. (15) is used to specify the bi-modal log-normal volume size distribution, whereas Eqs. (19)–(21) are not used. Thus, the user must specify the fine mode volume fraction $f_v = V_f/V$, where $V = V_f + V_c$, the volume mode radii $r_{\mathrm{v}f}$ and $r_{\mathrm{v}c}$ as well as the corresponding standard deviations σ_f and σ_c in addition to the refractive index of the particles relative to air (assumed to be the same for both modes).

In analogy to the liquid water content defined in Eq. (34) below, we may introduce the aerosol mass content (AMC) for each mode defined as

$$\mathrm{AMC} = \rho_{\mathrm{a}} \int_{r_{\min}}^{r_{\max}} \left(\frac{4\pi}{3}\right) r^3 n(r)\, dr \equiv \rho_{\mathrm{a}} f_{\mathrm{V}} \qquad [\mathrm{kg \cdot m^{-3}}] \tag{32}$$

where $n(r)$ is the aerosol size distribution $[\mathrm{m^{-3} \cdot m^{-1}}]$, ρ_{a} is the bulk aerosol density $[\mathrm{kg \cdot m^{-3}}]$, and f_{V} is the aerosol **volume fraction** (not to be confused with the fine mode volume fraction, f_v) given by:

$$f_{\mathrm{V}} \equiv \int_{r_{\min}}^{r_{\max}} \left(\frac{4\pi}{3}\right) r^3 n(r)\, dr = \mathrm{AMC}/\rho_{\mathrm{a}} \qquad \text{(dimensionless)}. \tag{33}$$

Typical values of atmospheric aerosol densities are $\rho_a \approx 1\,\mathrm{g}\cdot\mathrm{cm}^{-3} = 1\times10^{6}\,\mathrm{g}\cdot\mathrm{m}^{-3}$. Hence, an AMC value of $10^{-6}\,\mathrm{g}\cdot\mathrm{m}^{-3}$ would yield $f_V = 10^{-12}$.

3.3.5 Cloud IOPs (see clouds material)

Clouds consist of liquid water droplets or ice (frozen water) particles. The liquid water droplets making up warm clouds can be assumed to be spherical in shape, whereas ice crystals have a variety of non-spherical shapes. If we assume for simplicity that all cloud particles consist of spherical water droplets or spherical ice particles, we can use Mie theory to compute their IOPs because their refractive index is known. Hence, we may use Eqs. (29)–(31) to compute $\alpha_p(\lambda), \beta_p(\lambda)$, and $p_p(\lambda,\Theta)$ in much the same manner as we did for aerosols.

The real part of the refractive index of pure water needed in the Mie computations is adopted from Segelstein (1981) [25], while the imaginary part is calculated from the absorption coefficient $\alpha_w(\lambda)$ obtained from data published by Smith and Baker (1981) [26], Sogandares and Fry (1997) [27], Pope and Fry (1997) [28] for wavelengths between 340 and 700 nm, and by Kou et al. (1993) [29] for wavelengths between 720 and 900 nm.

It is customary to introduce the liquid water content (LWC) defined as

$$\mathrm{LWC} \equiv \rho_w \int_{r_{\min}}^{r_{\max}} \left(\frac{4\pi}{3}\right) r^3 n(r)\,dr \equiv \rho_w\, f_V \qquad [\mathrm{kg}\cdot\mathrm{m}^{-3}] \tag{34}$$

where $n(r)$ is the cloud droplet size distribution $[\mathrm{m}^{-3}\cdot\mathrm{m}^{-1}]$ and ρ_w is the liquid water mass density $[\mathrm{kg}\cdot\mathrm{m}^{-3}]$ and f_V stands for the dimensionless liquid (cloud) particle volume fraction defined in a similar manner as AMC in Eq. (33), i.e. $f_V = \mathrm{LWC}/\rho_w$. For a liquid water cloud a typical value of the LWC is about $0.5\,\mathrm{g}\cdot\mathrm{m}^{-3}$, implying that $f_V = 5\times10^{-7}$, for a density of water $\rho_w = 10^6\,\mathrm{g}\cdot\mathrm{m}^{-3}$. In Eq. (22) for the effective radius:

$$r_{\mathrm{eff}} = \frac{\int_{r_{\min}}^{r_{\max}} n(r) r^3\,dr}{\int_{r_{\min}}^{r_{\max}} n(r) r^2\,dr}$$

the numerator is proportional to the concentration or LWC, while the denominator is related to the scattering coefficient:

$$\beta_c = \int_0^\infty dr(\pi r^2) Q_\beta(r)\; n(r)\,dr \qquad [\mathrm{m}^{-1}].$$

If the size of the droplet is large compared to the wavelength λ, then $Q_\beta(r) \to 2$. Therefore, in the visible spectral range where $2\pi r/\lambda \gg 1$, we find:

$$\beta_c \approx \frac{3}{2}\frac{1}{\rho_w}\frac{\mathrm{LWC}}{r_{\mathrm{eff}}} = \frac{3}{2}\frac{f_V}{r_{\mathrm{eff}}} \qquad [\mathrm{m}^{-1}]. \tag{35}$$

For ice cloud particles assumed to be spherical in shape a similar expression for the scattering coefficient is obtained with f_V being the ice particle volume fraction. For a liquid water cloud with $f_V = 5\times10^{-7}$ and $r_{\mathrm{eff}} = 5\times10^{-6}\,\mathrm{m}$, we get $\beta_c = \frac{3}{2}\frac{f_V}{r_{\mathrm{eff}}} = 0.15\,\mathrm{m}^{-1}$, and hence an optical thickness of 15 for a 100 m thick cloud layer.

Parameterized cloud IOPs

Equation (35) suggests that cloud IOPs can be parameterized in terms of the effective radius and the volume fraction f_{V}. In fact, the cloud IOPs can be computed from the following simple algebraic expressions [30]:

$$\gamma_c/f_{\mathrm{V}} = a_1 r_{\mathrm{eff}}^{b_1} + c_1 \tag{36}$$

$$1 - \varpi_c = a_2 r_{\mathrm{eff}}^{b_2} + c_2 \tag{37}$$

$$g_c = a_3 r_{\mathrm{eff}}^{b_3} + c_3. \tag{38}$$

Here γ_c is the cloud extinction coefficient, $\varpi_c = \beta_c/\gamma_c$ is the single-scattering albedo, and g_c is the asymmetry factor. This parameterization scheme has not yet been implemented in AccuRT.

3.4 Snow and Ice IOPs (see snow and ice materials)

3.4.1 General Approach

Assuming that snow grains and sea ice inclusions consist of spherical particles, we may obtain their IOPs from Mie computations, which require the refractive index and the size distribution of the particles as input. Then, the inherent optical properties (IOPs), *i.e.* the absorption and scattering coefficients and the scattering phase function, $\alpha_{\mathrm{p}}(\lambda), \beta_{\mathrm{p}}(\lambda)$, and $p_{\mathrm{p}}(\lambda, \Theta)$, can be obtained from Eqs. (29)–(31). This approach leads to computed snow albedo values that agree surprisingly well with available observations. The following reasons why one does not make large errors by assuming spherical particles have been put forward by Craig Bohren as quoted by Grenfell et al. (1994) [31]: *The orientationally averaged extinction cross section of a convex particle that is large compared with the wavelength is one-half its surface area. The absorption cross section of a large, nearly transparent particle is proportional to its volume almost independent of its shape. The closer the real part of the particle's refractive index is to 1, the more irrelevant the particle shape. The asymmetry parameter of a large particle is dominated by near-forward scattering, which does not depend greatly on particle shape.* Based on these arguments, two options are provided:

1. Direct Mie calculations based on user-specified information about the particle refractive index and size assuming a lognormal size distribution;

2. A fast, yet accurate parameterization based on Mie calculations.

Direct Mie calculations (see snow and ice materials)

For this option we assume that snow grains and ice inclusions (air bubbles and brine pockets) consist of homogeneous spheres with a single-mode log-normal volume size distribution [see Eq. (15)], and we use the refractive index data base for ice compiled by Warren and Brandt (2008) [32]. The user specifies the effective radius r_{eff} and the width of the distribution σ, from which the geometrical mean radius r_{n} is computed

using Eq. (27). $r_{\rm n}$ and σ constitute the only input required for the Mie code described in Section 3.3.4, which will compute absorption and scattering coefficients as well the scattering phase function. An option to use only the first moment of the scattering phase function in conjunction with the Henyey-Greenstein scattering phase function is also provided. This option is useful because the Mie scattering phase function is unrealistic for non-spherical snow grains and ice inclusions.

Parameterization based on Mie calculations (see snow and ice materials) Sea ice optical properties were described by Jin et al. (1994) [33], and refined by Hamre et al. (2004) [34] and Jiang et al. (2005) [35]. Here we follow the most recent development of Stamnes et al. (2011) [36], who created a generic tool [**ISIOP**] for computing ice/snow IOPs (τ, ϖ, and g). The **ISIOP** tool can be used to generate ice/snow IOPs for any desired wavelength from ice/snow physical parameters: real and imaginary parts of the ice/snow refractive index, brine pocket concentration and effective size (sea ice), air bubble concentration and effective size (sea ice), volume fraction and absorption coefficient of sea ice impurities, asymmetry factors for scattering by snow grains, brine pockets, and air bubbles, and sea ice thickness.

For a specific value of r, we can compute $Q'_\alpha(r)$, $Q'_\beta(r)$, and $p_{\rm p}(\lambda,\Theta,r)$ using Mie theory, but evaluation of Eqs. (29)–(31) requires knowledge of the particle size distribution $n(r)$, which is usually unknown. Eqs. (29)–(31) can be considerably simplified by making the following assumptions [36]:

- The particle distribution is characterized by an effective radius given by Eq. (22), which obviates the need for an integration over r.

- The particles are weakly absorbing, so that

$$Q'_\alpha(r) \equiv Q'_\alpha \approx \frac{16\pi\, r_{\rm eff}\, \tilde{m}_{i,\rm p}}{3\lambda} \frac{1}{m_{\rm rel}} [m_{\rm rel}^3 - (m_{\rm rel}^2 - 1)^{3/2}] \tag{39}$$

  where $\tilde{m}_{i,\rm p}$ is the imaginary part of the refractive index of the particle, λ is the wavelength in vacuum, and $m_{\rm rel} = \tilde{m}_{r,\rm p}/\tilde{m}_{r,\rm med}$ is the ratio of the real part of the refractive index of the particle ($\tilde{m}_{r,p}$) to that of the surrounding medium ($\tilde{m}_{r,\rm med}$).

- The particles are large compared to the wavelength ($2\pi r/\lambda \gg 1$) which implies

$$Q'_\beta(r) \equiv Q'_\beta = 2. \tag{40}$$

  The scattering phase function may be represented by the one-parameter Henyey-Greenstein scattering phase function, which depends only on the asymmetry factor

$$g \equiv \langle \cos\Theta \rangle = \frac{1}{2} \int_{-1}^{1} p(\Theta) \cos\Theta \, d(\cos\Theta). \tag{41}$$

With these assumptions, Eqs. (29)–(31) become:

$$\alpha_{\rm p}(\lambda) = \alpha(\lambda)\frac{1}{m_{\rm rel}}\Big[1-(m_{\rm rel}^2-1)^{3/2}\Big]f_{\rm V} \tag{42}$$

$$\beta_{\rm p}(\lambda) = \frac{3}{2}\frac{f_{\rm V}}{r_{\rm eff}} \tag{43}$$

$$p_{\rm p}(\lambda,\Theta) = \frac{1-g^2}{(1+g^2-2g\cos\Theta)^{3/2}}. \tag{44}$$

Here $\alpha(\lambda) = 4\pi\tilde{m}_{i,\rm p}/\lambda$ is the absorption coefficient of the material of which the particle is composed, and $f_{\rm V} \equiv \frac{4\pi}{3}\int n(r)r^3dr \approx \frac{4}{3}\pi r_{\rm eff}^3 n_{\rm e}$, where $n_{\rm e} = \#$ of particles per unit volume with radius $r_{\rm eff}$. Note that Eq. (43) is identical to Eq. (35). Thus, it is clear that $f_{\rm V}$ represents the volume fraction of the particles as defined in Eq. (33). Typical values of $f_{\rm V}$ for air bubbles and brine pockets in sea ice are shown in Fig. 1.

As can be seen from Fig. 2, in a narrow wavelength range around 2,800 nm $m_{\rm rel} < 1.0$. Then Q'_α [Eq. (39)] and $\alpha_{\rm p}$ [Eq. (42)] will become complex numbers. To mitigate this problem, we take the absolute value of Q'_α and $\alpha_{\rm p}$ using complex arithmetic.

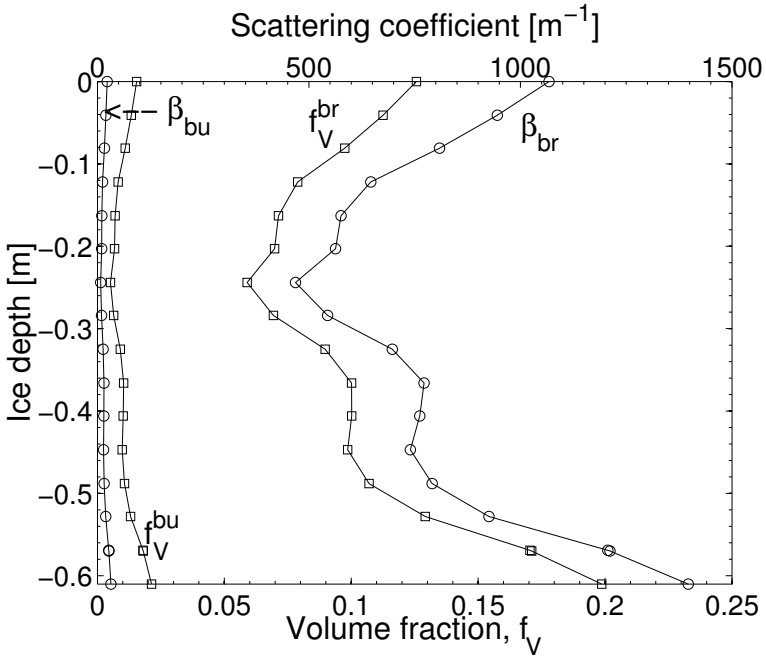

Figure 1: Volume fraction of brine pockets ($f_{\rm V}^{\rm br}$) and air bubbles ($f_{\rm V}^{\rm bu}$) (squares). Scattering coefficients of brine pockets ($\beta_{\rm br}$) and air bubbles ($\beta_{\rm bu}$) (circles). The two curves to the left represent air bubbles, and the two curves to the right represent brine pockets. After Hamre et al. (2004) [34]).

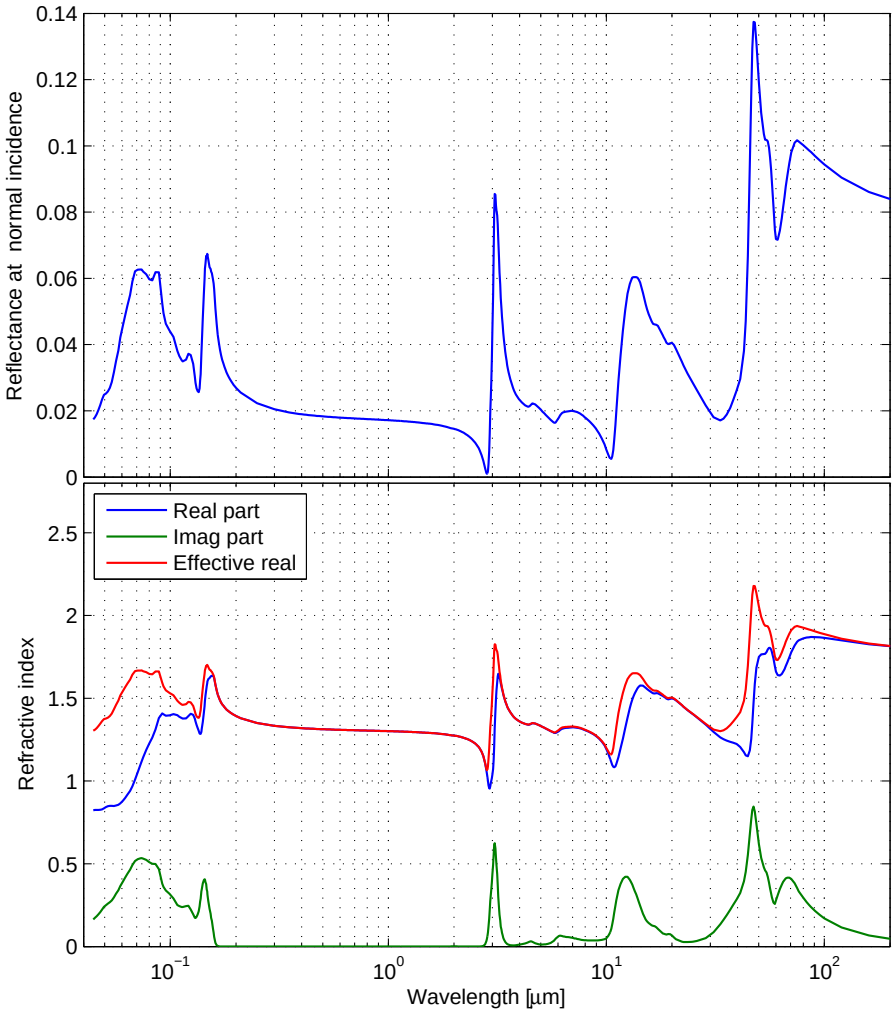

Figure 2: Upper panel: Spectral reflectance at normal incidence from an air-ice interface. Lower panel: Real part, imaginary part, and effective real value of the refractive index (see Section 4.1.2).

3.4.2 Extension of particle IOP parameterization to longer wavelengths

For wavelengths $\lambda \leq 1.2$ μm, the absorption and scattering efficiency for snow grains, brine inclusions in sea ice, and air bubbles in ice may be parameterized by Eqs. (39) and (40), and the asymmetry factor g can be held constant with wavelength and set equal to 0.85, 0.89, and 0.997 for air bubbles, snow grains, and brine pockets, respectively, and we may use the Henyey-Greenstein scattering phase function in Eq. (44). To extend the validity to near infrared wavelengths, we may use the following modified parameterizations, which are based in part on fits to results from Mie calculations [36]:

$$Q_\alpha = 0.94[1 - \exp(-Q'_\alpha/0.94)]; \qquad Q_\beta = 2 - Q_\alpha; \qquad g = g_0^{(1-Q_\alpha)^{0.6}} \tag{45}$$

where Q'_α is given by Eq. (39). Here g is the asymmetry factor of the scattering phase function, and g_0 is the asymmetry factor for non-absorbing particles. For large particles ($r > \sim 50$ μm) g_0 depends only on the real part of the refractive index. For a medium consisting of several absorbing and scattering constituents the total absorption and scattering efficiencies are just the sum of those due to the separate constituents. The optical thickness τ and single-scattering albedo ϖ for a slab of thickness h become [36]:

$$\tau = \pi r_{\text{eff}}^2 N h (Q_\alpha + Q_\beta); \qquad \varpi = \frac{Q_\beta}{Q_\alpha + Q_\beta} \tag{46}$$

where N is the total number of particles per unit volume, and Q_α and Q_β are the total absorption and scattering efficiencies, each equal to the sum of those due to the separate constituents. In highly scattering media such as snow and sea ice we may use the Henyey-Greenstein scattering phase function

$$p(\cos\Theta) = \frac{1 - g^2}{(1 + g^2 - 2g\cos\Theta)^{3/2}} \tag{47}$$

where g is the asymmetry parameter ($-1 < g < 1$) and Θ the scattering angle, to describe the angular scattering behavior. The modified parameterizations, which are represented by the dash-dot curves in Fig. 3 (Parameterizion 2), work well for all wavelengths for Q_α, while for Q_β and g they work well for wavelengths shorter than about 2.8 μm, but deviate significantly from predictions by Mie theory for longer wavelengths. Thus, for wavelengths longer than 2.8 μm one should preferably use results from the computationally less efficient Mie theory. Note that for wavelengths shorter than 2.8 μm, where the parameterizations work well, the variations in $\tilde{m}_{r,\text{p}}$ and $\tilde{m}_{i,\text{p}}$ are large. Thus, one would expect these parameterizations to be representative for most types of large particles [36].

3.4.3 Impurities, air bubbles, brine pockets, and snow

If the volume fraction of impurities within a snow grain or brine pocket is not too large, which is the case for typical situations occurring in nature, scattering by impurities can be ignored, so that their effects can be included by simply adding the imaginary part $\tilde{m}_{i,\text{imp}}$ of the refractive index for impurities to $\tilde{m}_{i,\text{p}}$ in Eq. (39). For typical impurities in snow and ice, the wavelength dependence of $\tilde{m}_{i,\text{imp}}$ can be parameterized as

$$\tilde{m}_{i,\text{imp}}(\lambda) = \tilde{m}_{i,\text{imp}}(\lambda_0)\,(\lambda_0/\lambda)^\eta \tag{48}$$

where η would be close to zero for black carbon, but larger for other impurities, and $\tilde{m}_{i,\text{imp}}(\lambda_0 = 440\,\text{nm})$ has values that depend on the type of impurity. Equation (48) is based on the observation that non-algal impurities tend to have a smooth increase towards shorter wavelengths in the absorption coefficient [37, 38, 39, 40], which is connected to the imaginary part of the refractive index through $\alpha = 4\pi\,\tilde{m}_{i,\text{imp}}/\lambda$. For snow, the number of snow grain particles per unit volume is $N = \frac{1}{\frac{4}{3}\pi r_{\text{eff}}^3}\frac{\rho_\text{s}}{\rho_\text{i}}$, where

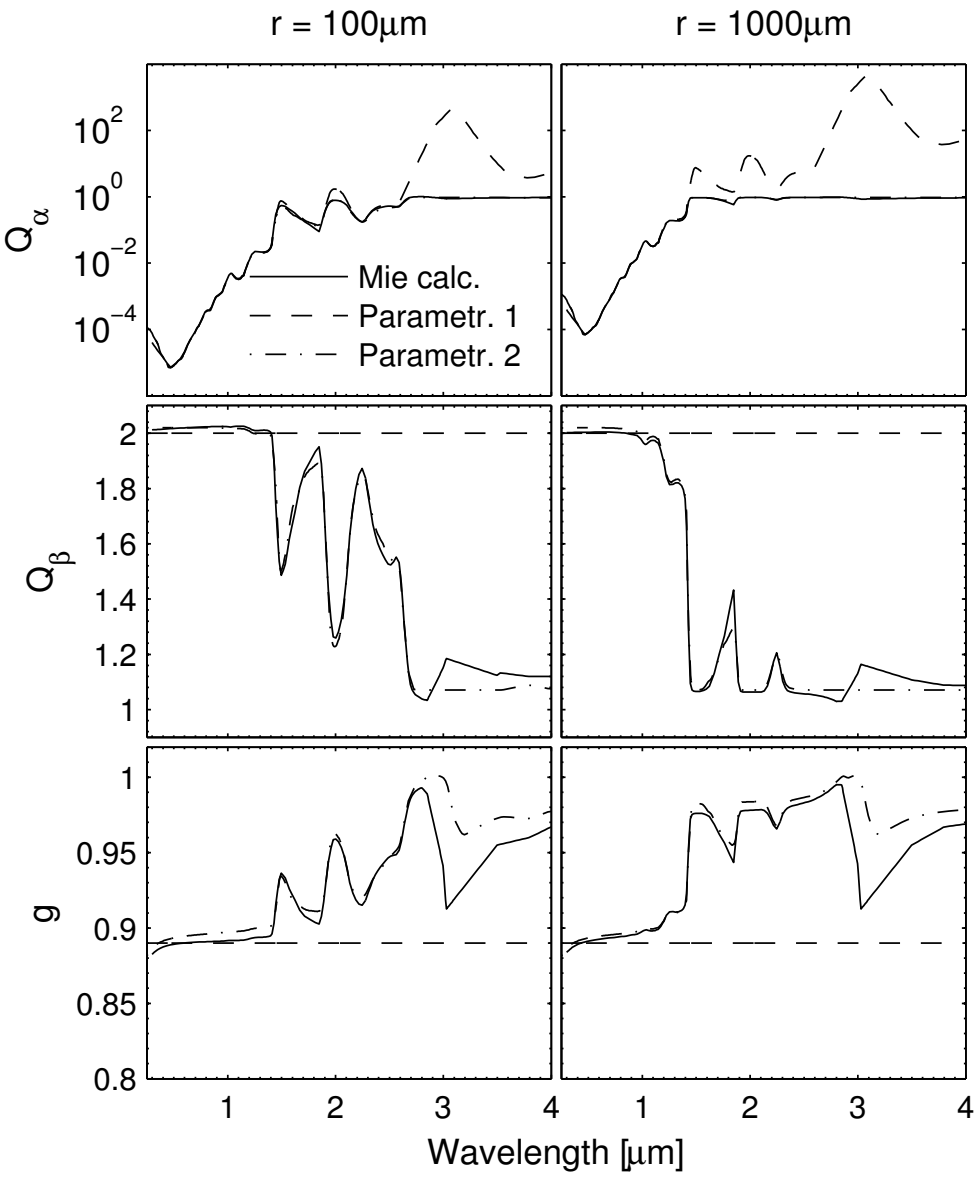

Figure 3: Comparisons of IOPs calculated using Mie theory with those obtained using Parameterization 1 [Eqs. (39)], which is valid for wavelengths shorter than about 1.2 μm [34], and Parameterization 2 [Eqs. (45)], which is valid also in the near infrared for $\lambda < 2.8$ μm (adapted from Stamnes et al., 2011 [36]).

r_{eff} is the effective particle radius, while ρ_{s} and ρ_{i} are the mass densities of snow and pure ice, respectively. The optical thickness and the single-scattering albedo can be calculated from Eqs. (45) and (46), using the refractive indices of pure ice [32] and impurities [Eq. (48)]. We assumed that sea ice consists of pure ice with embedded brine pockets, air bubbles, and impurities. To include the effects of the embedded

components, we first calculated the absorption coefficient α for sea ice

$$\alpha = \pi r_{\rm br}^2 N_{\rm br} Q_{\alpha,\rm br} + \left[1 - \frac{4}{3}\pi r_{\rm br}^3 N_{\rm br} - \frac{4}{3}\pi r_{\rm bu}^3 N_{\rm bu}\right] \frac{4\pi(\tilde{m}_{i,\rm p} + f_{\rm imp}\tilde{m}_{i,\rm imp})}{\lambda} \tag{49}$$

where $f_{\rm imp}$ is the volume fraction of impurities, $N_{\rm br}$ and $N_{\rm bu}$ are the number concentrations of brine pockets and air bubbles, respectively, $r_{\rm br}$ and $r_{\rm bu}$ are the corresponding effective radii, and $Q_{\alpha,\rm br}$ is the absorption efficiency for brine pockets. The two terms on the right side of Eq. (49) represent the absorption coefficients of brine pockets and surrounding ice (including impurities), respectively. In Eq. (49), we have used the general relation $\alpha = 4\pi\,\tilde{m}_{i,\rm p}/\lambda$, where λ is the wavelength in vacuum, and the expression inside the square brackets is the volume fraction of the ice surrounding all brine pockets and bubbles.

The air bubbles were assumed to be non-absorbing ($Q_{\alpha,\rm bu} = 0$), and the impurities were assumed to be uniformly distributed in the ice with $\tilde{m}_{i,\rm p}$ and $\tilde{m}_{i,\rm imp}$ being the imaginary parts of the refractive indices for pure ice and impurities, respectively. For brine pockets, which are in the liquid phase, the refractive index of sea water was used. The volume fraction $f_{\rm imp}$ of impurities typically lies in the range between 1×10^{-7} and 1×10^{-5}. The scattering coefficient β of sea ice is given by

$$\beta = \beta_{\rm br} + \beta_{\rm bu}; \quad \beta_{\rm br} = \pi r_{\rm br}^2 N_{\rm br} Q_{\beta,\rm br}; \quad \beta_{\rm bu} = \pi r_{\rm bu}^2 N_{\rm bu} Q_{\beta,\rm bu} \tag{50}$$

where $\beta_{\rm br}$ and $\beta_{\rm bu}$ are the scattering coefficients for brine pockets and air bubbles, respectively, and $Q_{\beta,\rm br}$ and $Q_{\beta,\rm bu}$ are the corresponding scattering efficiencies. Here we have ignored the scattering coefficient for pure sea ice because it is very small compared to either $\beta_{\rm br}$ or $\beta_{\rm bu}$. The optical thickness τ, the single-scattering albedo ϖ, and the asymmetry factor g for sea ice now become

$$\tau = (\alpha + \beta)h; \qquad \varpi = \frac{\beta}{\alpha + \beta}; \qquad g = \frac{\beta_{\rm br} g_{\rm br} + \beta_{\rm bu} g_{\rm bu}}{\beta_{\rm br} + \beta_{\rm bu}} \tag{51}$$

where h is the sea ice thickness.

3.5 Water IOPs – Bio-optical Models

In open ocean water, it is customary to assume that the **IOP**s of particulate matter can be parameterized in terms of the chlorophyll concentration. In coastal waters, we assume that the IOPs depend on the presence of inorganic (mineral) particles, organic (algae) particles, and Colored Dissolved Organic Matter **CDOM** in addition to pure water. Here we adopt a bio-optical model used in the CoastColour Round Robin (**CCRR**) effort, described in the document "Coastcolor-RRP-V1.2.doc" [41].

3.5.1 The pure_water material for pure water IOPs

As mentioned in Section 3.3.5, for pure water we adopt the real part of the refractive index of pure water from Segelstein (1981), and we use the absorption coefficient $\alpha_{\rm w}(\lambda)$ based on data published by Smith and Baker (1981) [26], Sogandares and

Fry (1997) [27], Pope and Fry (1997) [28] for wavelengths between 340 and 700 nm, and by Kou et al. (1993) [29] for wavelengths between 720 and 900 nm. Pure water scattering coefficients $\beta_w(\lambda)$ are based on data published by Morel (1974) [6], and the Rayleigh scattering phase function is given by Eq. (10) with depolarization ratio $\rho = 0.09$, and thus $f = (1-\rho)/(1+\rho) = 0.835$ (see Section 3.2.1).

3.5.2 The water_impurity_ccrr material

The CCRR bio-optical model [41] consists of the 3 input parameters CHL, MIN, and $\alpha_{CDOM}(443)$, which are allowed to vary. As currently implemented, the CCRR model may be used for wavelengths between 280 and 900 nm. The absorption by algae particles is extrapolated below 400 nm and above 700 nm as indicated in Fig. 4. It should be noted that according to this decomposition into three basic components, the "mineral particle" component can include also non-algae particles whose absorption does not covary with that of the algae particles. [41]

Mineral particles (see water_impurity_ccrr material)

The absorption coefficient for mineral particles at 443 nm is given by (Babin et al., 2003a) [42][†]:

$$\alpha_{MIN}(443) = 0.041 \times 0.75 \times \text{MIN}$$

and its spectral variation is described by (Babin et al., 2003a [42]; data file provided by CCRR [41]):

$$\alpha_{MIN}(\lambda) = \alpha_{MIN}(443)[\exp(-0.0123(\lambda - 443))]. \tag{52}$$

The scattering coefficient at 555 nm is given by (Babin et al., 2003b [43]):

$$\beta_{MIN}(555) = 0.51 \times \text{MIN}$$

and the spectral variation of the attenuation coefficient is (data file from CCRR [41]):

$$\gamma_{MIN}(\lambda) = \gamma_{MIN}(555) \times (\lambda/\lambda_0)^{-c}; \qquad c = 0.3749, \qquad \lambda_0 = 555\,\text{nm} \tag{53}$$

where

$$\begin{aligned}\gamma_{MIN}(555) &= \alpha_{MIN}(555) + \beta_{MIN}(555) \\ &= [0.041 \times 0.75 \exp(-0.0123(555-443)) + 0.51] \times \text{MIN} = 0.52 \times \text{MIN}.\end{aligned}$$

The spectral variation of the scattering coefficient for mineral particles follows from

$$\beta_{MIN}(\lambda) = \gamma_{MIN}(\lambda) - \alpha_{MIN}(\lambda). \tag{54}$$

The average Petzold phase function with a backscattering ratio of 0.026, as tabulated by Mobley (1994) [2], is used to describe the scattering phase function for mineral particles.

[†]Note on units: $\alpha_{MIN}(\lambda)/\text{MIN} = 0.041$ has units $[\text{m}^2\text{g}^{-1}]$, so that if MIN has units of $[\text{g m}^{-3}]$, then the units of $\alpha_{MIN}(\lambda)$ will be $[\text{m}^{-1}]$.

Algae particles (see water_impurity_ccrr material)

The absorption coefficient for *pigmented* particles (algae particles or phytoplankton) can be written (Bricaud et al., 1998 [44]):

$$\alpha_{\rm pig}(\lambda) = A_\phi(\lambda) \times [\rm CHL]^{E_\phi(\lambda)} \tag{55}$$

where $A_\phi(\lambda)$ and $E_\phi(\lambda)$ are given by Bricaud et al. (1998) [44], and where CHL is the chlorophyll concentration, which represents the concentration of pigmented particles (algae particles or phytoplankton). The functions $A_\phi(\lambda)$ and $E_\phi(\lambda)$ are displayed in Fig. 4. The attenuation coefficient for pigmented particles at 660 nm

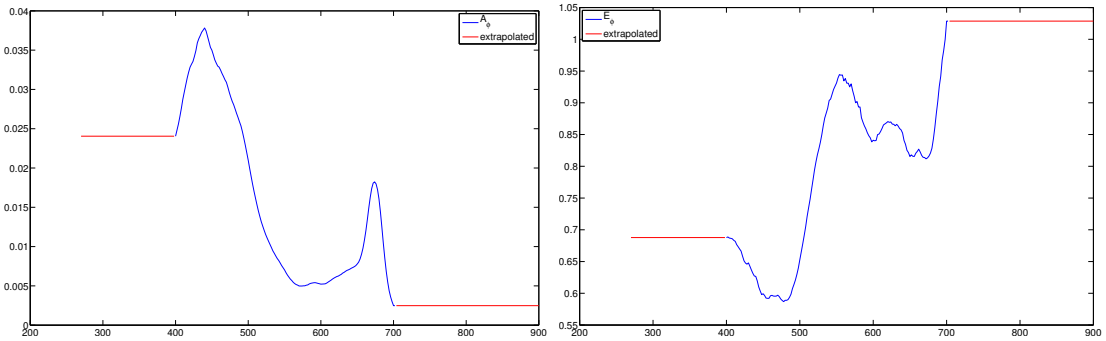

Figure 4: Spectral variation of the numerical coefficients $A_\phi(\lambda)$ (left) and $E_\phi(\lambda)$ (right) in Eq. (55). The blue color indicates original data provided by Bricaud et al. (1998) [44]. The red color indicates extrapolated values.

is given by (Loisel and Morel, 1998 [45]):

$$\gamma_{\rm pig}(660) = \gamma_0 \times [\rm CHL]^\eta; \qquad \gamma_0 = 0.407; \qquad \eta = 0.795$$

and its spectral variation is taken to be (Morel et al., 2002 [46]):

$$\gamma_{\rm pig}(\lambda) = \gamma_{\rm pig}(660) \times (\lambda/660)^\nu \tag{56}$$

where

$$\nu = \begin{cases} 0.5 \times [\log_{10} \rm CHL - 0.3] & 0.02 < \rm CHL < 2.0 \\ 0 & \rm CHL > 2.0. \end{cases}$$

The spectral variation of the scattering coefficient for pigmented particles follows from the difference:

$$\beta_{\rm pig}(\lambda) = \gamma_{\rm pig}(\lambda) - \alpha_{\rm pig}(\lambda). \tag{57}$$

The scattering phase function for pigmented particles is assumed to be described by the Fournier-Forand phase function (see below) with a backscattering ratio equal to 0.006 (Mobley et al., 2002 [47], Morel et al., 2002 [46]).

Colored Dissolved Organic Matter (CDOM) (see water_impurity_ccrr material)

The absorption by CDOM is given by (Babin et al., 2003b [43]):

$$\alpha_{\text{CDOM}}(\lambda) = \alpha_{\text{CDOM}}(443) \times \exp[-0.0176(\lambda - 443)]. \tag{58}$$

Total Absorption and Scattering Coefficients (see water_impurity_ccrr material)

The total absorption and scattering coefficients due to water impurities for the CCRR IOP model are given by:

$$\alpha_{\text{tot}}(\lambda) = \alpha_{\text{MIN}}(\lambda) + \alpha_{\text{pig}}(\lambda) + \alpha_{\text{CDOM}}(\lambda) \tag{59}$$

$$\beta_{\text{tot}}(\lambda) \equiv \beta_{\text{p}}(\lambda) = \beta_{\text{MIN}}(\lambda) + \beta_{\text{pig}}(\lambda). \tag{60}$$

Scattering Phase Function for Particles (see water_impurity_ccrr material)

Many measurements have shown that the particle size distribution (PSD) function in oceanic water can be accurately described by an inverse power law (Junge distribution) $F(r) = C_r/r^{\xi}$, where $F(r)$ is the number of particles per unit volume per unit bin width, and r [μm] is the radius of the assumed spherical particle. C_r [$\text{cm}^{-3} \cdot \mu\text{m}^{\xi-1}$] is the Junge coefficient, and ξ is the PSD slope, which typically varies between 3.0 and 5.0 (Diehl and Haardt, 1980 [48]; McCave, 1983 [49]). By assuming an inverse power law (Junge distribution) for the PSD, Fournier and Forand (1994) [50] derived an analytic expression for the scattering phase function of oceanic water (hereafter referred to as the FF scattering phase function). This FF scattering phase function is given by (Mobley et al., 2002) [47]

$$p_{\text{FF}}(\Theta) = \frac{1}{4\pi(1-\delta)^2\delta^{\nu}}\left\{\nu(1-\delta) - (1-\delta^{\nu}) + \frac{4}{u^2}[\delta(1-\delta^{\nu}) - \nu(1-\delta)]\right\} + \frac{1-\delta_{180}^{\nu}}{16\pi(\delta_{180}-1)\delta_{180}^{\nu}}[3\cos^2\Theta - 1] \tag{61}$$

where $\nu = 0.5(3-\xi)$, $u = 2\sin(\Theta/2)$, $\delta \equiv \delta(\Theta) = \frac{u^2}{3(\tilde{m}_r-1)^2}$, $\delta_{180} = \delta(\Theta = 180^{\circ}) = \frac{4}{3(\tilde{m}_r-1)^2}$, Θ is the scattering angle, and $\tilde{m}_r$ is the real part of the refractive index.

Setting $x = \cos\Theta$, and integrating the FF scattering phase function over the backward hemisphere, one obtains the backscattering ratio or backscatter fraction defined in Eq. (9), *i.e.* [47]

$$b_{\text{FF}} = \frac{1}{2}\int_{\pi/2}^{\pi} p_{\text{FF}}(\cos\Theta)\sin\Theta\, d\Theta = \frac{1}{2}\int_0^1 p_{\text{FF}}(-x)\, dx$$
$$= 1 - \frac{1-\delta_{90}^{\nu+1} - 0.5(1-\delta_{90}^{\nu})}{(1-\delta_{90})\delta_{90}^{\nu}} \tag{62}$$

where $\delta_{90} = \delta(\Theta = 90^\circ) = \frac{4}{3(\tilde{m}_r - 1)^2} \sin^2(45^\circ) = \frac{2}{3(\tilde{m}_r - 1)^2}$. Equation (62) can be solved for ν in terms of $b_{\rm FF}$ and δ_{90}, implying that ν and thus ξ can be determined if the real part of the refractive index $\tilde{m}_r$ and the backscatter ratio $b_{\rm FF}$ are specified. As a consequence, the FF scattering phase function can be evaluated from a measured value of $b_{\rm FF}$ if the real part of the refractive index $\tilde{m}_r$ is known.

To describe the angular variation of the scattering, we use the FF scattering phase function for phytoplankton and the Rayleigh scattering phase function [Eq. (10)] for scattering by pure water. It was shown by Mobley et al. (2002) [47] that with proper choices of $\tilde{m}_r$ and ξ the FF scattering phase function is an excellent proxy for the well-known Petzold (1972) [51] measurements. In a previous study, Li et al. (2008) [52] used $\tilde{m}_r = 1.0686$, and $\xi = 3.38$, which correspond to a backscattering ratio of 0.0056 [see Fig. 2 in Mobley et al. (2002) [47]]. As noted by Mobley at al. (2002) [47], this choice of $\{\tilde{m}_r, \xi\}$ values is consistent with a certain mixture of living microbes and resuspended sediments. As already mentioned, in the **CCRR** bio-optical model adopted here, the Petzold scattering phase function with a backscattering ratio of 0.026 is used to represent mineral (non-algal) particles. These scattering phase functions are shown in Fig. 5. We use the moment-fitting

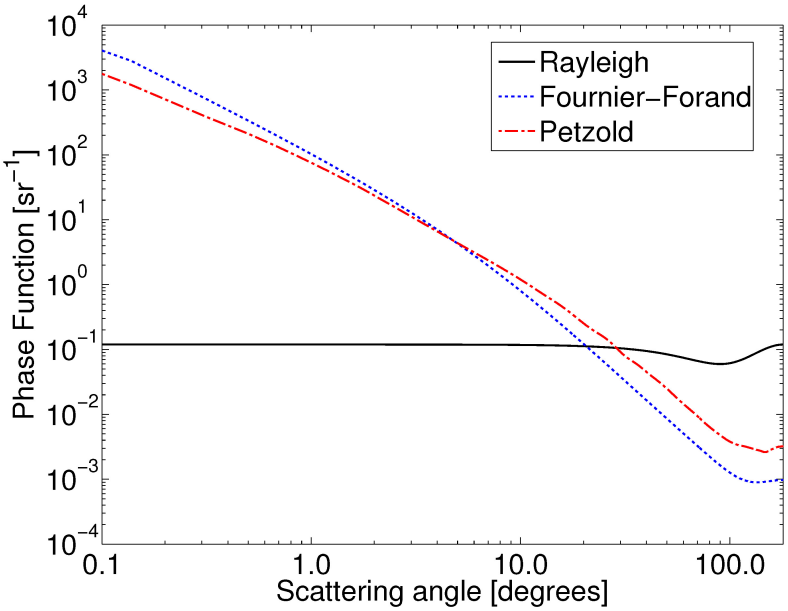

Figure 5: Rayleigh, Fournier-Forand and Petzold phase functions used to represent scattering by water molecules, pigmented particles, and non-algal particles, respectively, in AccuRT.

program of Hu et al. (2000) [24] to create Legendre expansion coefficients $\chi_{\ell,\rm PET}$ and $\chi_{\ell,FF}$ for the Petzold and FF scattering phase functions. Thus, the **IOP** total scattering phase function Legendre expansion coefficients are given by:

$$\chi_\ell = \frac{\beta_{\rm pig}(\lambda)\chi_{\ell,\rm FF} + \beta_{\rm MIN}(\lambda)\chi_{\ell,\rm PET} + \beta_{\rm w}(\lambda)\chi_{\ell,\rm water}}{\beta_{\rm pig}(\lambda) + \beta_{\rm MIN}(\lambda) + \beta_{\rm w}(\lambda)}. \tag{63}$$

Thus, in the **water_impurity_ccrr** material of **AccuRT** the user must specify the 3 input parameters CHL, MIN, and $\alpha_{\rm CDOM}(443)$ in addition to the vertical location of the impurities. Optimally a profile of CHL, MIN, and CDOM with depth may be provided that will automatically linearly interpolate the impurities to fit the layers specified in the **main** configuration file.

3.5.3 The water_impurity_sbc and water_impurity_gsm materials

Based on field measurements obtained in the Santa Barbara Channel (SBC) and compiled in the NOMAD data base (Werdell and Bailey, 2005 [53]), Li et al. (2008) [52] constructed a bio-optical model for the SBC coastal waters. Although this SBC bio-optical model is not a general model, it is representative for a coastal water scenario. Another frequently used bio-optical model is the GSM model (Garver et al., 1997 [54], Maritorena et al., 2002 [55]), which is included in NASA's SeaDAS software package. GSM is a global model which has the same structure as the SBC model, but with different coefficients.

In the SBC model, the water body, in addition to pure water, is assumed to be described by 3 parameters that can be varied (and thus retrieved): the chlorophyll concentration [CHL] (which represents the concentration of pigmented particles), the CDOM absorption coefficient at 443 nm [$\alpha_{\rm CDOM}(443)$], and the total scattering coefficient at 443 nm [$\beta_{\rm tot}(443)$]. The IOPs of the SBC model are described by:

$$\alpha_{\rm pig}^{\rm SBC}(\lambda) = a_1^{\rm SBC}(\lambda)[{\rm CHL}]^{a_2(\lambda)} \tag{64}$$

$$\alpha_{\rm CDOM}^{\rm SBC}(\lambda) = \alpha_{\rm CDOM}^{\rm SBC}(443)\exp[-0.012(\lambda-443)] \tag{65}$$

$$\beta_{\rm tot}^{\rm SBC}(\lambda) = \beta_{\rm tot}^{\rm SBC}(443)(\lambda/443). \tag{66}$$

Similarly, for the GSM model the IOPs are described by

$$\alpha_{\rm pig}^{\rm GSM}(\lambda) = a_1^{\rm GSM}(\lambda)[{\rm CHL}] \tag{67}$$

$$\alpha_{\rm CDOM}^{\rm GSM}(\lambda) = \alpha_{\rm CDOM}^{\rm GSM}(443)\exp[-0.0206(\lambda-443)] \tag{68}$$

$$\beta_{\rm tot}^{\rm GSM}(\lambda) = \beta_{\rm tot}^{\rm GSM}(443)(\lambda/443)^{1.0337}. \tag{69}$$

Note that the wavelength dependent factors $a_1^{\rm SBC}(\lambda)$ and $a_2(\lambda)$ in Eq. (64) as well as $a_1^{\rm GSM}(\lambda)$ in Eq. (67) are determined from field measurements compiled in the NOMAD data base. For simplicity we will assume here that $\alpha_{\rm pig}^{\rm SBC}(\lambda) = \alpha_{\rm pig}^{\rm GSM}(\lambda) \equiv \alpha_{\rm pig}^{\rm CCRR}(\lambda)$, so that the difference between the 3 models lies in the treatment of scattering and CDOM absorption.

For both the SBC and GSM models, CDOM represents a combination of colored dissolved organic matter and mineral particles. Hence, values of $\alpha_{\rm CDOM}^{\rm SBC}(443)$ in Eq. (65) and $\alpha_{\rm CDOM}^{\rm GSM}(443)$ in Eq. (68) should be compared to the sum $\alpha_{\rm CDOM}^{\rm CCRR}(443) + 0.041 \times 0.75$ MIN. The total suspended particle scattering coefficient is $\beta_{\rm tot}^{\rm SBC}(\lambda)$ and $\beta_{\rm tot}^{\rm GSM}(\lambda)$ in the SBC and GSM model, respectively, each being comparable to $\beta_{\rm tot}(\lambda) = \beta_{\rm MIN}(\lambda) + \beta_{\rm pig}(\lambda)$ in the CCRR model.

The most significant difference between these 3 models is that the SBC and GSM models do not separately include mineral particles although the total scattering

coefficient does include the total suspended particle scattering. Another difference is that the CCRR model is based on three different reference wavelengths, namely 443 nm for $\alpha_{\rm MIN}$, 555 nm for $\gamma_{\rm MIN}$, and 660 nm for $\alpha_{\rm pig}$, while the SBC and the GSM models are based only on 443 nm as a reference wavelength.

3.6 Vacuum material

This material has refractive index $\tilde{m}_{c,\rm vac} = \tilde{m}_{r,\rm vac} + i\tilde{m}_{i,\rm vac} = 1.0$, and no absorption or scattering. It is useful for simulating a transparent slab (atmosphere or water). If selected as the only material in the lower slab, that slab will be transparent with refractive index 1.0. If selected as the first of several materials in the lower slab, then that slab will have refractive index 1.0, but the scattering and absorption properties will be as specified separately.

3.7 Spectral averaging of absorption coefficients

Since the the scattering coefficient is a smooth function of wavelength, no spectral averaging is necessary. In contrast, the absorption coefficient varies rapidly and erratically with wavelength making spectral averaging necessary.

3.7.1 The Chandrasekhar Mean

The TOA solar irradiance decreases rapidly with (decreasing) wavelength for $\lambda <$ 350 nm, and the ozone absorption cross section increases rapidly between 350 nm and 250 nm. The steep gradients in the solar irradiance and ozone absorption cross section suggest that it may be useful to define a mean absorption cross section (called the Chandrasekhar Mean [3]) by weighting it with the extraterrestrial solar irradiance $F_0(\lambda)$ as follows:

$$\langle \alpha_n \rangle \equiv \frac{\int_{\lambda_1}^{\lambda_2} \alpha_n(\lambda) F_0(\lambda)\, d\lambda}{\int_{\lambda_1}^{\lambda_2} F_0(\lambda)\, d\lambda}. \tag{70}$$

For rapid energy budget calculations the spectral resolution adopted in k-distribution band models [3] is a useful option that will be included in future versions of **AccuRT**.

3.7.2 Absorption by atmospheric gases

The TOA solar irradiance $F_0(\lambda)$ will be attenuated due to absorption by gases in the atmosphere. The transmitted solar irradiance in the nadir direction at atmospheric depth level ℓ (with $\ell = 0$ at the TOA) can be expressed as:

$$F_\ell(\lambda) = F_0(\lambda)\, e^{-\tau_\ell(\lambda)}. \tag{71}$$

Hence, the atmospheric transmittance at level ℓ becomes

$$\mathcal{T}_\ell(\lambda) = \frac{F_\ell(\lambda)}{F_0(\lambda)} = e^{-\tau_\ell(\lambda)} \tag{72}$$

and the corresponding optical depth is

$$\tau_\ell(\lambda) = -\ln[\mathcal{T}_\ell(\lambda)]. \tag{73}$$

The irradiance measured by an instrument at level ℓ with spectral response function $w(\lambda)$ and bandwidth $\Delta\lambda$ can be written

$$F_\ell^{\Delta\lambda} = \frac{\int_{\Delta\lambda} w(\lambda) F_\ell(\lambda)\, d\lambda}{\int_{\Delta\lambda} w(\lambda)\, d\lambda} = \frac{\int_{\Delta\lambda} w(\lambda) F_0(\lambda)\mathcal{T}_\ell(\lambda)\, d\lambda}{\int_{\Delta\lambda} w(\lambda)\, d\lambda} = \int_{\Delta\lambda} \tilde{w}(\lambda) F_0(\lambda)\mathcal{T}_\ell(\lambda)\, d\lambda \tag{74}$$

where $\tilde{w}(\lambda) = w(\lambda)/\int_{\Delta\lambda} w(\lambda) d\lambda$ is the "normalized" response function. Since $\mathcal{T}_0(\lambda) = 1$ (at TOA), the band-weighted transmittance at level ℓ becomes:

$$\mathcal{T}_\ell^{\Delta\lambda} = \frac{F_\ell^{\Delta\lambda}}{F_0^{\Delta\lambda}} = \frac{\int_{\Delta\lambda} \tilde{w}(\lambda) F_0(\lambda)\mathcal{T}_\ell(\lambda)\, d\lambda}{\int_{\Delta\lambda} \tilde{w}(\lambda) F_0(\lambda)\, d\lambda}. \tag{75}$$

Hence, the band-weighted absorption optical depth at level ℓ becomes:

$$\tau_\ell^{\Delta\lambda} = -\ln[\mathcal{T}_\ell^{\Delta\lambda}]. \tag{76}$$

In **gasIOP** the band-weighted transmittance given by Eq. (75) is evaluated numerically using a spectral resolution of 1 cm^{-1}.

3.7.3 Absorption by aerosol and cloud particles

Aerosol and cloud particles are assumed to consist of a polydispersion of homogeneous spheres with a specified wavelength-dependent refractive index. Since Mie computations are computing-intensive, Mie-computed absorption coefficients are tabulated at user-specified center wavelengths, and linear interpolation is used to obtain the absorption coefficient within the user-specified bandwidth of the center wavelength.

3.7.4 Absorption by pure ice, ice impurities, ice inclusions (brine pockets and bubbles) and snow grains

For pure ice, tabulated values of the imaginary part of the refractive index $\tilde{m}_i$ [32] are used to compute the absorption coefficient ($\alpha = 4\pi\,\tilde{m}_i/\lambda$), and linear interpolation is used to obtain the average absorption coefficient within the user-specified bandwidth. Impurities (*e.g.* algae and soot) are assumed to be uniformly distributed within the ice and the absorption is given in terms of a user-specified imaginary part of the refractive index. Brine pockets and air bubbles embedded in the ice as well as snow grains are assumed to be spherical particles. For the direct Mie calculation option, Mie-computed absorption coefficients are tabulated at user-specified center wavelengths, and linear interpolation is used to obtain the average absorption coefficient within the user-specified bandwidth. For the parameterized option, we use the absorption coefficient of snow/ice particles given by Eq. (42), which depends on the refractive index of ice. We use tabulated data for the real and the imaginary

part of the refractive index of ice as a function of wavelength [32] and linear interpolation to obtain values between wavelength grid points. The absorption coefficient is computed by Eq. (42) at 100 evenly spaced wavelengths within the user-specified bandwidth, and then the average value is computed.

3.7.5 Absorption by liquid water

We use tabulated data for the absorption coefficient of pure water as a function of wavelength [28, 29] and linear interpolation to obtain values between tabulated wavelength grid points. The absorption coefficient is obtained at 100 evenly spaced wavelengths within the user-specified wavelength bandwidth using linear interpolation between tabulated values, and then the average is computed. The absorption coefficient due to impurities in water is computed from a bio-optical model [see Eq. (59)] at user-specified center wavelengths, and linear interpolation is used to obtain the average absorption coefficient within the user-specified bandwidth.

3.7.6 Solar spectrum

The solar spectrum is also averaged over 100 evenly spaced wavelengths within each user-specified wavelength bandwidth.

Please note that a more accurate (but also more computationally demanding) way to average over a bandwidth is to compute radiances or irradiances at many monochromatic wavelengths, and then average the computed quantities.

4 Radiative Transfer

4.1 Radiative Transfer Equation – unpolarized case

Consider a *coupled* system consisting of two adjacent slabs (atmosphere overlying a water body) separated by a plane, horizontal interface across which the refractive index changes abruptly from a value $\tilde{m}_{c,1}$ in one of the slabs (hereafter slab$_1$ will refer to the atmosphere) to a value $\tilde{m}_{c,2}$ in the other slab (hereafter slab$_2$ will refer to a water body). If the **IOP**s in each of the two slabs vary only in the vertical direction denoted by z, where z increases upward, the corresponding vertical optical depth, denoted by $\tau(z)$, is defined by

$$\tau(z) = \int_z^\infty [\alpha(z') + \beta(z')]\, dz' \tag{77}$$

where the absorption and scattering coefficients α and β are defined in Eqs. (1) and (2). Note that the vertical optical depth is defined to increase downward from $\tau(z = \infty) = 0$ at the top of the atmosphere. In either of the two slabs, assumed to be in local thermodynamic equilibrium so that they emit radiation according to

the local temperature $T(\tau(z))$, the diffuse radiance distribution $I(\tau, u, \phi)$ can be described by the radiative transfer equation (RTE)

$$\mu \frac{dI(\tau, u, \phi)}{d\tau} = I(\tau, u, \phi) - S(\tau, u', \phi') \tag{78}$$

where

$$S(\tau, u', \phi') = S^*(\tau, u', \phi') - [1 - \varpi(\tau)]B(\tau) \\ - \frac{\varpi(\tau)}{4\pi} \int_0^{2\pi} d\phi' \int_{-1}^{1} p(\tau, u', \phi'; u, \phi) I(\tau, u', \phi') du'. \tag{79}$$

Here u is the cosine of the polar angle θ, ϕ is the azimuth angle, $\varpi(\tau) = \beta(\tau)/[\alpha(\tau) + \beta(\tau)]$ is the single-scattering albedo, $p(\tau, u', \phi'; u, \phi)$ is the scattering phase function defined by Eq. (6), and $B(\tau)$ is the thermal radiation field given by the Planck function. The differential vertical optical depth is [see Eq. (77)]

$$d\tau(z) = -[\alpha(\tau) + \beta(\tau)]\, dz \tag{80}$$

where the minus sign indicates that τ increases in the downward direction, whereas z increases in the upward direction, as noted above. The scattering angle Θ and the polar and azimuth angles are related by

$$\hat{\mathbf{\Omega}}' \cdot \hat{\mathbf{\Omega}} = \cos\Theta = \cos\theta\, \cos\theta' + \sin\theta'\, \sin\theta\, \cos(\phi' - \phi).$$

By definition, $\theta = 180^\circ$ is directed toward nadir (straight down) and $\theta = 0^\circ$ toward zenith (straight up). Thus, $u = \cos\theta$ varies in the range $[-1, 1]$ (from nadir to zenith). For cases of oblique illumination of the system, $\phi = 180^\circ$ is defined to be the azimuth angle of the incident light.

The single-scattering source term $S^*(\tau, \mu', \phi')$ in Eq. (79) in slab$_1$ (with complex refractive index $\tilde{m}_{c,1} = \tilde{m}_{r,1} + i\tilde{m}_{i,1}$) is different from that in the lower slab (slab$_2$, with refractive index $\tilde{m}_{c,2} = \tilde{m}_{r,2} + i\tilde{m}_{i,2}$). In slab$_1$ it is given by

$$S_1^*(\tau, u, \phi) = \frac{\varpi(\tau) F_0}{4\pi} p(\tau, -\mu_0, \phi_0; u, \phi) e^{-\tau/\mu_0} \\ + \frac{\varpi(\tau) F_0}{4\pi} \rho_{\mathrm{F}}(-\mu_0; \tilde{m}_{c,1}, \tilde{m}_{c,2}) p(\tau, \mu_0, \phi_0; u, \phi) e^{-(2\tau_1 - \tau)/\mu_0}, \tag{81}$$

where τ_1 is the vertical optical depth of the atmosphere, $\rho_{\mathrm{F}}(-\mu_0; \tilde{m}_{c,1}, \tilde{m}_{c,2})$ is the Fresnel reflectance at the slab$_1$-slab$_2$ interface, $\mu_0 = \cos\theta_0$, with θ_0 being the zenith or polar angle of the incident beam of illumination, and where $\tilde{m}_{r,2} > \tilde{m}_{r,1}$. Note that the real part of the refractive index of the medium in slab$_1$ has been assumed to be smaller than that of the medium in slab$_2$, as would be the case for air overlying a water body. The first term on the right-hand side of Eq. (81) is due to first-order scattering of the attenuated incident beam of irradiance F_0 (normal to the beam), while the second term is due to first-order scattering of the attenuated incident beam that is reflected at the slab$_1$-slab$_2$ interface. In slab$_2$ the single-scattering

source term consists of the attenuated incident beam that is refracted through the interface, *i.e.*

$$S_2^*(\tau,u,\phi) = \frac{\varpi(\tau)F_0}{4\pi}\frac{\mu_0}{\mu_{0n}}\mathcal{T}_{\rm F}(-\mu_0;\tilde{m}_{c,1},\tilde{m}_{c,2}) \\ \times\ p(\tau,-\mu_{0n},\phi_0;u,\phi)e^{-\tau_1/\mu_0}e^{-(\tau-\tau_a)/\mu_{0n}}, \tag{82}$$

where $\mathcal{T}_{\rm F}(-\mu_0;\tilde{m}_{c,1},\tilde{m}_{c,2})$ is the Fresnel transmittance through the interface, and μ_{0n} is the cosine of the polar angle θ_{0n} in slab$_2$, which is related to $\theta_0 = \arccos\mu_0$ by Snell's law.

For a two-slab system with source terms as given by Eqs. (81) and (82), a solution based on the discrete-ordinate method [56, 57] of the RTE in Eq. (78) subject to appropriate boundary conditions at the top of slab$_1$, at the bottom of slab$_2$, and at the slab$_1$-slab$_2$ interface, was first developed by Jin and Stamnes [58] (see also Thomas and Stamnes [3]).

4.1.1 Isolation of azimuth dependence

The azimuth dependence in Eq. (78) may be isolated by expanding the scattering phase function in *Legendre polynomials*, $P_\ell(\cos\Theta)$, and making use of the addition theorem for spherical harmonics [3]

$$p(\cos\Theta) \;=\; p(u',\phi';u,\phi) = \sum_{m=0}^{2N-1}(2-\delta_{0,m})p^m(u',u)\,\cos m(\phi'-\phi), \tag{83}$$

where $\delta_{0,m}$ is the Kronecker delta, *i.e.* $\delta_{0,m}=1$ for $m=0$ and $\delta_{0,m}=0$ for $m\neq 0$, and

$$p^m(u',u) = \sum_{\ell=m}^{2N-1}(2l+1)\chi_\ell\Lambda_\ell^m(u')\Lambda_\ell^m(u). \tag{84}$$

Here

$$\chi_\ell = \frac{1}{2}\int_{-1}^{1}P_\ell(\cos\Theta)p(\cos\Theta)\,d(\cos\Theta) \tag{85}$$

is an expansion coefficient and $\Lambda_\ell^m(u)$ is given by

$$\Lambda_\ell^m(u) \equiv \sqrt{\frac{(\ell-m)!}{(\ell+m)!}}P_\ell^m(u) \tag{86}$$

where $P_\ell^m(u)$ is an associated Legendre polynomial of order m. Expanding the radiance in a similar way,

$$I(\tau,u,\phi) = \sum_{m=0}^{2N-1}I^m(\tau,u)\,\cos m(\phi-\phi_0), \tag{87}$$

where ϕ_0 is the azimuth angle of the incident light, one finds that each Fourier component satisfies the following RTE (see Thomas and Stamnes [3] for details)

$$\mu\frac{dI^m(\tau,u)}{d\tau} \;=\; I^m(\tau,u) - \frac{\varpi(\tau)}{2}\int_{-1}^{1}p^m(\tau,u',u)\,I^m(\tau,u)\,d\mu - S^{*m}(\tau,u), \tag{88}$$

where $m=0,1,2,\ldots,2N-1$ and $p^m(\mu',\mu)$ is given by Eq. (84).

4.1.2 The interface between the two slabs

When a beam of light is incident upon a plane interface between two slabs of different refractive indices, one fraction of the incident light will be reflected and another fraction will be transmitted or refracted. For unpolarized light incident upon the interface between the two slabs, the Fresnel reflectance ρ_{F} is given by

$$\rho_{\mathrm{F}} = \frac{1}{2}(\rho_{\perp} + \rho_{\parallel}) \tag{89}$$

where $\rho_{\perp}$ is the reflectance for light polarized with the electric field perpendicular to the plane of incidence, and $\rho_{\parallel}$ is the reflectance for light polarized with the electric field parallel to the plane of incidence [3, 59, 60]. Thus, one finds

$$\rho_{\mathrm{F}} = \frac{1}{2}\left[\left|\frac{\mu_1 - m_{\mathrm{rat}}\mu_t}{\mu_1 + m_{\mathrm{rat}}\mu_2}\right|^2 + \left|\frac{\mu_2 - m_{\mathrm{rat}}\mu_1}{\mu_2 + m_{\mathrm{rat}}\mu_1}\right|^2\right], \tag{90}$$

where $\mu_1 \equiv \mu_{\mathrm{air}} = \cos\theta_1$, θ_1 being the angle of incidence, $\mu_2 \equiv \mu_{\mathrm{ocn}} = \cos\theta_2$, θ_2 being the angle of refraction determined by Snell's law ($\tilde{m}_{r,1}\sin\theta_1 = \tilde{m}_{r,2}\sin\theta_2$), and $m_{\mathrm{rat}} = \tilde{m}_{c,2}/\tilde{m}_{c,1}$. Similarly, the Fresnel transmittance becomes

$$\mathcal{T}_{\mathrm{F}} = 2m_{\mathrm{rel}}\mu_i\mu_t\left[\left|\frac{1}{\mu_i + m_{\mathrm{rat}}\mu_t}\right|^2 + \left|\frac{1}{\mu_t + m_{\mathrm{rat}}\mu_i}\right|^2\right], \tag{91}$$

where $m_{\mathrm{rel}} = \tilde{m}_{r,2}/\tilde{m}_{r,1}$.

Effective refractive index

For light normally incident on a plane interface between air and water or air and ice with complex refractive index $\tilde{m}_c$ (assuming $\tilde{m}_{\mathrm{air}} = 1.0$), the reflectance is given by

$$\rho_{\mathrm{F}} = \frac{1}{2}(\rho_{\perp} + \rho_{\parallel}) = \left|\frac{\tilde{m}_c - 1}{\tilde{m}_c + 1}\right|^2. \tag{92}$$

For most wavelengths of solar radiation reaching the surface of the Earth, the imaginary part of $\tilde{m}_c$ for liquid water or ice is very small, implying that we may assume $\tilde{m}_c$ to have a real value larger than 1.0. However, at some wavelength bands in the near infrared the real part of $\tilde{m}_c$ may be less than 1.0, and the imaginary part of $\tilde{m}_c$ may be sufficiently large to have an influence on the reflectance and transmittance. To account for this influence we may use an effective real refractive index $\tilde{m}_{\mathrm{eff}}$ which, when substituted for $\tilde{m}_c$ in Eq. (92), gives the correct reflectance at normal incidence. Substituting $\tilde{m}_c = \tilde{m}_{\mathrm{eff}}$ in Eq. (92), we find

$$\tilde{m}_{\mathrm{eff}} = \frac{1 + \sqrt{\rho_{\mathrm{F}}}}{1 - \sqrt{\rho_{\mathrm{F}}}} \tag{93}$$

where ρ_{F} is obtained from Eq. (92) with the correct complex refractive index $\tilde{m}_c$. Note that $\tilde{m}_{\mathrm{eff}}$ equals the real part of $\tilde{m}_c$ for most wavelengths. As can be seen from Fig. 2, for wavelengths in the solar spectrum between 300 nm and 4,000 nm the real part of the refractive index is larger than 1.0 except for a narrow wavelength range around 2,800 nm in which the imaginary part is non-zero.

4.2 Discrete-Ordinate Solution of the RTE – unpolarized case

To solve Eq. (88) for a coupled (two-slab) system one needs to take into account the boundary conditions at the top of slab$_1$ and at the bottom of slab$_2$ as well as the reflection and transmission at the slab$_1$-slab$_2$ interface. In addition, the radiation field must be continuous across interfaces between horizontal layers with different **IOP**s within each of the two slabs (with constant refractive index). Such horizontal layers are introduced to resolve vertical variations in the **IOP**s within each slab.

The integro-differential RTE [Eq. (88)] may be transformed into a system of coupled, ordinary differential equations by using the discrete-ordinate approximation to replace the integral in Eq. (88) by a quadrature sum consisting of $2N_1$ terms in slab$_1$ and $2N_2$ terms in slab$_2$, where N_1 terms are used to represent the radiance in different directions in the downward hemisphere in slab$_1$ that refracts through the interface into slab$_2$. In slab$_2$, N_2 terms are used to represent the radiance in the downward hemisphere. Note that $N_2 > N_1$ because additional terms are needed in slab$_2$ with real part of the refractive index $\tilde{m}_{r,2} > \tilde{m}_{r,1}$ to represent the downward radiance in directions inside the region of total internal reflection.

Seeking solutions to the discrete ordinate approximation of Eq. (88), one obtains the Fourier component of the radiance at any vertical position both in slab$_1$ and slab$_2$. The solution for the pth layer of slab$_1$ is given by (dropping the superscript m) [3]

$$I_p(\tau, \pm\mu_i^t) = \sum_{j=1}^{N_1} \left\{ C_{-jp} g_{-jp}^t(\pm\mu_i^t) e^{k_{jp}^t \tau} + C_{+jp} g_{jp}^t(\pm\mu_i^t) e^{-k_{jp}^t \tau} + U_p(\tau, \pm\mu_i^t) \right\} \tag{94}$$

where $\pm\mu_i \equiv \pm|u_i|$, $i = 1, \ldots, N_1$ and p is less than or equal to the number of layers in slab$_1$. The solution for the qth layer of slab$_2$ is given by [3]

$$I_q(\tau, \pm\mu_i^b) = \sum_{j=1}^{N_2} C_{-jq} g_{-jq}^b(\pm\mu_i^b) e^{k_{jq}^b \tau} + C_{+jq} g_{jq}^b(\pm\mu_i^b) e^{-k_{jq}^b \tau} + U_q(\tau, \pm\mu_i^b) \tag{95}$$

where $i = 1, \ldots, N_2$. The superscripts ^{t} and ^{b} are used to denote *top* slab$_1$ and *bottom* slab$_2$ parameters, respectively, the plus (minus) sign is used for radiances streaming upward (downward), and $k_{jp}^t, g_{jp}^t, k_{jq}^b$, and g_{jq}^b are eigenvalues and eigenvectors determined by the solution of an algebraic eigenvalue problem, which results when one seeks a solution of the homogeneous version of Eq. (88) (with $S^{*m}(\tau, u) = 0$) in the discrete-ordinate approximation. The terms $U_p(\pm\mu_i^t)$ and $U_q(\pm\mu_i^b)$ are the particular solutions. The coefficients $C_{\pm jp}$ and $C_{\pm jq}$ are determined by boundary conditions at the top of slab$_1$ and at the bottom of slab$_2$, the continuity of the basic radiance (the radiance divided by the square of the real part of the refractive index) at each interface between internal layers in each of the slabs, and Fresnel's equations at the slab$_1$-slab$_2$ interface.

The numerical code **AccuRT** [58, 61] computes radiances at any optical depth, polar, and azimuth angle by solving the RTE in Eq. (88) for each layer of the two

slabs by using the discrete-ordinate method to convert the integro-differential RTE into a system of coupled ordinary differential equations. The **AccuRT** method can be summarized as follows:

1. Slab_1 and slab_2 are separated by a plane interface at which the refractive index changes from $\tilde{m}_{c,1} = \tilde{m}_{r,1} + i\tilde{m}_{i,1}$ in slab_1 to $\tilde{m}_{c,2} = \tilde{m}_{r,2} + i\tilde{m}_{i,2}$ in slab_2, where $\tilde{m}_{c,2}$ depends on the wavelength.

2. Each of the two slabs is divided into a sufficiently large number of homogenous horizontal layers to adequately resolve the vertical variation in its IOPs.

3. Fresnel's equations for the reflectance and transmittance are applied at the slab_1-slab_2 interface, in addition to the law of reflection and Snell's Law to determine the magnitude and directions of the reflected and refracted rays.

4. Discrete-ordinate solutions to the RTE are computed separately for each layer in the two slabs.

5. Finally, boundary conditions at the top of slab_1 and the bottom of slab_2 are applied, in addition to continuity conditions at layer interfaces within each of the two slabs.

Fourier components of the radiances at a vertical location given by the pth layer in slab_1 or the qth layer in slab_2 are computed from Eqs. (94)-(95), and the azimuth-dependent diffuse radiance distribution from Eq. (87). Upward and downward hemispherical irradiances and scalar irradiances are then calculated by integrating the azimuthally-averaged (zeroth-order, $m = 0$) Fourier component $I_p^0(\tau, +\mu_i)$ or $I_p^0(\tau, -\mu_i)$ over polar angles.

The downward **hemispherical** irradiance $E^t(\tau)$ and downward **scalar** irradiance $\mathcal{I}^t(\tau)$ in slab_1 consist of direct components E^t_{dir} and $\mathcal{I}^t_{\text{dir}}$, respectively, given by

$$E^t_{\text{dir}}(\tau) = \mu_0 F_0 e^{-\tau/\mu_0} \quad \text{and} \quad \mathcal{I}^t_{\text{dir}}(\tau) = F_0 e^{-\tau/\mu_0} \tag{96}$$

and diffuse components $E^t_{\text{d,diff}}$ and $\mathcal{I}^t_{\text{d,diff}}$

$$E^t_{\text{d,diff}}(\tau) = 2\pi \int_0^1 I^{t,0}_{\text{d,diff}}(\tau, \mu)\mu \, d\mu \quad \text{and} \quad \mathcal{I}^t_{\text{d,diff}}(\tau) = 2\pi \int_0^1 I^{t,0}_{\text{d,diff}}(\tau, \mu) \, d\mu \tag{97}$$

where $I^{t,0}_{\text{d,diff}}(\tau, \mu)$ is the azimuthally-averaged diffuse downward radiance at optical depth $\tau \le \tau_1$ in slab_1. Similarly, the upward diffuse irradiance $E^t_{\text{u,diff}}$ and the upward diffuse scalar irradiance $\mathcal{I}^t_{\text{u,diff}}$ in slab_1 are

$$E^t_{\text{u,diff}}(\tau) = 2\pi \int_0^1 I^{t,0}_{\text{u,diff}}(\tau, \mu)\mu \, d\mu \quad \text{and} \quad \mathcal{I}^t_{\text{u,diff}}(\tau) = 2\pi \int_0^1 I^{t,0}_{\text{u,diff}}(\tau, \mu) \, d\mu \tag{98}$$

and the net hemispherical irradiance $E^t_{\text{net}}(\tau)$, and total scalar irradiance $\mathcal{I}^t_{\text{tot}}(\tau)$, are

$$E^t_{\text{net}}(\tau) = E^t_{\text{u,diff}}(\tau) - [E^t_{\text{dir}}(\tau) + E^t_{\text{d,diff}}(\tau)] \quad \text{and} \quad \mathcal{I}^t_{\text{tot}}(\tau) = \mathcal{I}^t_{\text{dir}}(\tau) + \mathcal{I}^t_{\text{d,diff}}(\tau) + \mathcal{I}^t_{\text{u,diff}}(\tau). \tag{99}$$

In slab$_2$, the corresponding downward (direct and diffuse), upward, and net (total) irradiances become:

$$E^b_{\rm dir}(\tau) = \mu_0 F_0 e^{[-\tau_1/\mu_0 - \tau/\mu_{0n}]} \quad \text{and} \quad \mathcal{I}^b_{\rm dir}(\tau) = F_0 e^{[-\tau_1/\mu_0 - \tau/\mu_{0n}]} \tag{100}$$

$$E^b_{\rm d,diff}(\tau) = 2\pi \int_0^1 I^{b,0}_{\rm d,diff}(\tau,\mu)\mu\, d\mu \quad \text{and} \quad \mathcal{I}^b_{\rm d,diff}(\tau) = 2\pi \int_0^1 I^{b,0}_{\rm d,diff}(\tau,\mu)\, d\mu \tag{101}$$

$$E^b_{\rm u,diff}(\tau) = 2\pi \int_0^1 I^{b,0}_{\rm u,diff}(\tau,\mu)\mu\, d\mu \quad \text{and} \quad \mathcal{I}^b_{\rm u,diff}(\tau) = 2\pi \int_0^1 I^{b,0}_{\rm u,diff}(\tau,\mu)\, d\mu \tag{102}$$

$$\begin{aligned} E^b_{\rm net}(\tau) &= E^b_{\rm u,diff}(\tau) - [E^b_{\rm dir}(\tau) + E^b_{\rm d,diff}(\tau)] \quad \text{and} \\ \mathcal{I}^b_{\rm tot}(\tau) &= \mathcal{I}^b_{\rm dir}(\tau) + \mathcal{I}^b_{\rm d,diff}(\tau) + \mathcal{I}^b_{\rm u,diff}(\tau) \end{aligned} \tag{103}$$

where the downward and upward azimuthally-averaged radiances in slab$_2$ are given by $I^{b,0}_{\rm d,diff}(\tau,\mu)$ and $I^{b,0}_{\rm u,diff}(\tau,\mu)$, and μ_{0n} is the cosine of the polar angle θ_{0n} in slab$_2$, which is related to $\theta_0 = \arccos\mu_0$ by Snell's law. The total scalar irradiance, which is simply 4π times the mean radiance ($\mathcal{I}_{\rm tot} = 4\pi\bar{I}$), is sometimes referred to as the **actinic flux** by photochemists, although we may want to avoid using the term **flux**, which should be reserved for the hemispherical flow of energy or momentum. Instead we may refer to the total scalar irradiance as the **actinic radiation field** to avoid confusion.

5 Summary

We have described a computational tool for radiative transfer simulations in a coupled system consisting of two adjacent horizontal slabs with different refractive indices. The computer code accounts for reflection and transmission at the interface between the two slabs, and allows for each slab to be divided into a number of layers sufficiently large to resolve the variation in the inherent optical properties (**IOP**s) with depth in each slab.

The user interface of the computer code is designed to make it easy to specify the required input including wavelength range, solar forcing, and layer-by-layer **IOP**s in each of the two slabs as well as the two types of desired output:

- irradiances and mean intensities (scalar irradiances) at a set of user-specified vertical positions in the coupled system;
- radiances in a number of user-specified directions at a set of user-specified vertical positions in the coupled system.

6 Acronyms

Air Material for absorption band model based on cross sections in the UV and visible spectral ranges

aerosols particulate matter in the atmosphere except cloud particles

AOP Apparent Optical Property

AccuRT Accurate Radiative Transfer Tool for Coupled Systems

CDOM Colored Dissolved Organic Matter

CCRR CoastColour Round Robin, http://www.coastcolour.org/round_robin.html

DISORT DIScrete Ordinate Radiative Transfer (code)

clouds particulate matter in the atmosphere: liquid water and ice particles in clouds

earth_atmospheric_gases profiles of atmospheric molecular absorption and scattering optical depths

gasIOP Band model for absorption by atmospheric gases

ice ice material

IOP Inherent Optical Property

ISIOP Tool for computing ice and snow IOPs

LowTran Low resolution (20 cm^{-1}) atmospheric transmittance code

materials Radiatively-significant constituents like gases and particles in the atmosphere and dissolved and particulate matter in the water

ModTran Moderate resolution (2 cm^{-1}) atmospheric transmittance code

NASA National Aeronautics and Space Administration

NOMAD NASA bio-Optical Marine Algorithm Data set

pure_water absorption and scattering by pure water

RTE Radiative Transfer Equation

SeaDAS SeaWiFS Database Analysis System

SeaWiFS Sea-viewing Wide Field-of-view Sensor

snow snow material

totabsCoef output; double precision; total water matter absorption coefficient [m^{-1}]

totscatCoef output; double precision; total water matter scattering coefficient [m^{-1}]

TOA top of the atmosphere

SBC Santa Barbara Channel

water_impurity_ccrr absorption and scattering by dissolved and particulate matter in the water

water_impurity_gsm absorption and scattering by dissolved and particulate matter in the water

water_impurity_sbc absorption and scattering by dissolved and particulate matter in the water

References

[1] Stamnes, K. and J. J. Stamnes, *Radiative Transfer in Coupled Environmental Systems*, Wiley-VCH, 2015.

[2] Mobley, C. D., *Light and Water: Radiative Transfer in Natural Waters*, Academic Press, San Diego, CA, 1994.

[3] Thomas, G. E. and K. Stamnes. *Radiative transfer in the atmosphere and ocean*, Cambridge University Press, 1999, second edition, 2002.

[4] Rayleigh, L. A re-examination of the light scattered by gases in respect of polarization. I. Experiments on the common gases, Proc. Roy. Soc. **97**, 435–450, 1920.

[5] Rayleigh, L. A re-examination of the light scattered by gases in respect of polarization. II. Experiments on helium and argon, Proc. Roy. Soc. **98**, 57–64 (1920).

[6] Morel, A., Optical properties of pure water and pure seawater, in Optical Aspects of Oceanography, N. G. Jerlov and E. S. Nielsen (eds.), pp. 1–24, Academic, San Diego, Calif., 1974.

[7] Morel, A. and B. Gentili, Diffuse reflectance of oceanic waters: its dependence on sun angle as influenced by the molecular scattering contribution, Appl. Opt. **30**, 4427–4437, 1991.

[8] Rayleigh, L. On the light from the sky, its polarization and colour, Phil. Mag. **41**, 107–120, 274–279, 447–454, 1871.

[9] Henyey, L. C. and J. L. Greenstein, Diffuse radiation in the galaxy, Astrophys J. **93**, 70-83, 1941.

[10] Anderson, G. P., S. A. Clough, F. X. Kneizys, J. H. Chetwynd and E. P. Shettle, AFGL Atmospheric Constituent Profiles (0-120 km). *AFGL-TR-86-0110 (OPI)*. Hanscom AFB, MA 01736, 1986.

[11] Ahmad, Z., B. A. Franz, C. R. McClain, E. J. Kwiatkowska, J. Werdell, E. P. Shettle, and B. N. Holben, New aerosol models for the retrieval of aerosol optical thickness and normalized water-leaving radiances from the SeaWiFS and MODIS sensors over coastal regions and open oceans, Appl Opt. **49**, 5545-5560, 2010.

[12] Hess, M., P. Koepke, and I. Schult, Optical properties of aerosols and clouds: The software package OPAC, Bulletin of the American Meteorological Society **79**, 831 - 844, 1998.

[13] Gordon, H. R., and M. Wang, Retrieval of water-leaving radiance and aerosol optical thickness over the oceans with Sea-WiFS: a preliminary algorithm, Appl. Opt. **33**, 443–452, 1994.

[14] Gordon, H. R., Atmospheric correction of ocean color imagery in the Earth Observation System era, J. Geophys. Res. **102**, 17081-17106, 1997.

[15] Davies, C. N., Size distribution of atmospheric particles, J. Aerosol Sci. **5**, 293-300, 1974.

[16] Holben, B. N., T. F. Eck, I. Slutsker, D. Tanre, J. P. Buis, A. Setzer, E. Vermote, J. A. Reagan, Y. Kaufman, T. Nakajima, F. Lavenu, I. Jankowiak, and A. Smirnov, AERONET – A federated instrument network and data archive for aerosol characterization, Remote Sens. Environ. **66**, 1–16, 1998.

[17] Holben, B. N., D. Tanre, A. Smirnov, T. F. Eck, I. Slutsker, N. Abuhassan, W. W. Newcomb, J. Schafer, B. Chatenet, F. Lavenue, Y. J. Kaufman, J. Vande Castle, A. Setzer, B. Markham, D. Clark, R. Frouin, R. Halthore, A. Karnieli, N. T. O'Neill, C. Pietras, R. T. Pinker, K. Voss, and G. Zibordi, An emerging ground-based aerosol climatology: aerosol optical depth from AERONET, J. Geophys. Res. **106**, 12067-12097, 2001.

[18] Hänel, G., The properties of atmospheric aerosol particles as functions of the relative humidity at thermodynamic equilibrium with the surrounding moist air, in Advances in Geophysics, H. E. Landsberg and J. V. Miehem, eds. (Academic), Vol. 19, 1976.

[19] E. P. Shettle and R. W. Fenn, Models for the Aerosols of the Lower Atmosphere and the Effects of Humidity Variations on their Optical Properties, AFGL-TR-79-0214 (Air Force Geophysics Laboratory, Hanscomb AFB, Mass., 1979).

[20] B. Yan, K. Stamnes, W. Li, B. Chen, J. J. Stamnes, and S. C. Tsay, Pitfalls in atmospheric correction of ocean color imagery: How should aerosol optical properties be computed? Appl. Opt. **41**, 412-423, 2002.

[21] Hansen, J. E. and L. D. Travis, Light scattering in planetary atmospheres, Space Sci. Rev., **16**, 527-610, 1974. doi:10.1007/BF00168069.

[22] Du, H., Mie-Scattering Calculation, Appl. Opt. **43**, 1951-1956, 2004.

[23] Copyright (C) 2011 Hans-Peter Schadler ⟨ hps@abyle.org ⟩.

[24] Hu, Y.-X., B. Wielicki, B. Lin, G. Gibson, S.-C. Tsay, K. Stamnes, and T. Wong, Delta-fit: A fast and accurate treatment of particle scattering phase functions with weighted singular-value decomposition least squares fitting, J. Quant. Spectrosc. Radiat. Transfer **65**, 681-690, 2000.

[25] Segelstein, D. J., The complex refractive index of water, M. S. Thesis – Department of Physics. University of Missouri-Kansas City, 1981.

[26] Smith, R. C. and K. S. Baker, Optical properties of the clearest natural waters (200-800nm), Appl. Opt. **20**, 177–184, 1981.

[27] Sogandares, F. M. and E. S. Fry, Absorption spectrum (340-640 nm) off pure water. I. Photothermal measurements, Appl. Opt. **36**, 8699–8709, 1997.

[28] Pope, R. M. and E. S. Fry, Absorption spectrum (380-700 nm) of pure water, II, Integrating cavity measurements, Appl. Opt. **36**, 8710 - 8723, 1997.

[29] Kou, L., D. Labrie, and P. Chylek, Refractive indices of water and ice in the 0.65 μm to 2.5 μm spectral range, Appl. Opt. **32**, 3531-3540, 1993.

[30] Hu, Y.-X., and K. Stamnes, An accurate parameterization of the radiative properties of water clouds suitable for use in climate models, J. Climate **6**, 728-742, 1993.

[31] Grenfell, T. S. , S. G. Warren, and P. C. Mullen, Spectral albedo of Antarctic snow, J. Geophys. Res. **99**, 18,669-84, 1994.

[32] Warren, S. G. and R. E. Brandt, Optical constants of ice from the ultraviolet to the microwave: A revised compilation, J. Geophys. Res. **113**, D14220, doi:10.1029/2007JD009744, 2008.

[33] Jin, Z., K. Stamnes, W. F. Weeks, and S. C. Tsay, The effect of sea ice on the solar energy budget in the atmosphere-sea ice-ocean system: A model study, J. Geophys. Res. **99**, 25281-25294, 1994.

[34] Hamre, B., J.-G. Winther, S. Gerland, J. J. Stamnes, and K. Stamnes, Modeled and measured optical transmittance of snow covered first-year sea ice in Kongsfjorden, Svalbard, J. Geophys. Res. **109**, d0i:10.1029/2003JC001926, 2004.

[35] Jiang, S., K. Stamnes, W. Li and B. Hamre, Enhanced Solar Irradiance Across the Atmosphere-Sea Ice Interface: A Quantitative Numerical Study, Appl. Opt. **44**, 2613-2625, 2005.

[36] Stamnes, K., B. Hamre, J. J. Stamnes, G. Ryzhikov, M. Birylina, R. Mahoney, B. Hauss, and A. Sei, Modeling of radiation transport in coupled atmosphere-snow-ice-ocean systems, J. Quant. Spectrosc. Radiat. Transfer **112**, 714-726, doi:10.1016/j.jqsrt.2010.06.006, 2011.

[37] Ackermann, M., et al. Optical properties of deep glacial ice at the South Pole, J. Geophys. Res. **111**, D13203, doi:10.1029/2005JD006687, 2006.

[38] Fialho, P., A. D. A. Hansen, R. E. Honrath, Absorption coefficients by aerosols in remote areas: A new approach to decouple dust and black carbon absorption coefficients using seven-wavelength Aethalometer data, Journal of Aerosol Science **36**, 267-282, 2005.

[39] Twardowski, M. S. , E. Boss, J. M. Sullivan, P. L. Donaghay, Modeling the spectral shape of absorption by chromophoric dissolved organic matter, Marine Chemistry **89**, 69-88, 2004.

[40] Uusikivi, J., et al., Contribution of mycosporine-like amino acids and colored dissolved and particulate matter to sea ice optical properties and ultraviolet attenuation, Limnol. Oceanogr. **55**, 703-713, 2010.

[41] Coastcolour: Round Robin Protocol, version 1.2, Brockmann Consult, October 5, 2010. – see also: http://www.coastcolour.org/round_robin.html.

[42] Babin, M., A. D. Stramski, G. M. Ferrari, H. Claustre, A. Bricaud, G. Obelesky, and N. Hoepffner, Variations in the light absorption coefficients of phytoplankton, nonalgal particles and dissolved organic matter in coastal waters around Europe, J. Geophys. Res. **108**, 3211, doi:10.1029/2001JC000882, 2003.

[43] Babin, M., A. Morel, V. Fournier-Sicre, F. Fell, and D. Stramski, Light scattering properties of marine particles in coastal and open ocean waters as related to the particle mass concentration, Limnol. Oceanogr. **28**, 843-859, 2003.

[44] Bricaud, A., A. Morel, M. Babin, K. Allali, and H. Claustre, Variations in light absorption by suspended particles with chlorophyll concentration in oceanic (case 1) waters: Analysis and implicatioons for bio-optical models, J. Geophys. Res. **103**, 31,033-31,044, 1998.

[45] Loisel, H., and A. Morel, Light scattering and chlorophyll concentration in case 1 waters: a re-examination, Limnol. Oceanogr. **43**, 847-857, 1998.

[46] Morel, A., D. Antoine, and B. Gentili, Bidirectional reflectance of oceanic waters: accounting for Raman emission and varying particle scattering phase function, Apl. Opt. **41**, 6289–6306, 2002.

[47] Mobley, C. D., L. K. Sundman, and E. Boss, Phase function effects on oceanic light fields, Appl. Opt. **41**, 1035–1050, 2002.

[48] Diehl, P. and H. Haardt, Measurement of the spectral attenuation to support biological research in a "plankton tube" experimiment, Oceanol. Acta **3**, 89-96, 1980.

[49] McCave, I. N. , Particulate size spectra, behavior, and origin of nephloid layers over the Nova Scotia continental rise, J. Geophys. Res. **88**, 7647–7660, 1983.

[50] Fournier, G. and J. L. Forand, Analytic phase function for ocean water. In Ocean Optics XII SPIE Vol. 2258, J. S. Jaffe (ed.), 194-201, 1994.

[51] Petzold, T. L., Volume scattering functions for selected ocean waters, Visibility Lab. Report, Scripps Inst. Oceanogr., SIO Ref. 72–78, 1972.

[52] Li, W., K. Stamnes, R. Spurr, and J. J. Stamnes, Simultaneous Retrieval of Aerosols and Ocean Properties: A Classic Inverse Modeling Approach. II. SeaWiFS Case Study for the Santa Barbara Channel, Int. J. Rem. Sens., DOI: 10.1080/01431160802007632 **29**, 5689-5698, 2008.

[53] Werdell, P. J. and S. W. Bailey, An improved in-situ bio-optical data set for ocean color algorithm development and satellite data product validation, Remote Sensing of Environment **98**, 122–140, 2005.

[54] Garver, S. A., and D. Siegel, Inherent optical property inversion of ocean color spectra and its biogeochemical interpretation 1. Time series from the Sargasso Sea, J. Geophys. Res. **102**, 18607–18625, 1997.

[55] Maritorena, S., D. A. Siegel, and A. R. Peterson, Optimization of a semi-analytical ocean color model for global-scale applications, Appl. Opt. **41**, 2705-2714, 2002.

[56] Stamnes, K., S. C. Tsay, W. J. Wiscombe, and K. Jayaweera, Numerically stable algorithm for discrete-ordinate-method radiative transfer in multiple scattering and emitting layered media, Appl. Opt. **27**, 2502–2509, 1988.

[57] Stamnes, K., S. C. Tsay, W. J. Wiscombe, and I. Laszlo, DISORT, A General-Purpose Fortran Program for Discrete-Ordinate-Method Radiative Transfer in Scattering and Emitting Layered Media: Documentation of Methodology, ftp://climate.gsfc.nasa.gov/pub/wiscombe/MultipleScatt/, 2000.

[58] Jin, Z. and K. Stamnes, Radiative transfer in nonuniformly refracting layered media: atmosphere-ocean system, Appl. Opt. **33**, 431–442, 1994.

[59] Bohren, C. F. and D. R. Huffman, *Absorption and Scattering by Small Particles*, John Wiley, New York, USA, 1983.

[60] Born, M. and E. Wolf, *Principles of Optics*, Cambridge University Press, 1980.

[61] Yan. B. and K. Stamnes, Fast yet accurate computation of the complete radiance distribution in the coupled atmosphere ocean system. J. Quant. Spectrosc. Radiat. Transfer **76**, 207–223, 2003.